A constrained solid-shell model for the geometric nonlinear finite-element analysis of laminates with alternating stiff/soft layers. Applications to laminated glass

A constrained solid-shell model for the geometric nonlinear finite-element analysis of laminates with alternating stiff/soft layers. Applications to laminated glass

Domenico Magisano[a], Leonardo Leonetti[a], Giovanni Garcea[a], Gianni Royer-Carfagni[b,c]

[a] *Department of Informatics, Modeling, Electronics and Systems Engineering, University of Calabria, 87030 Rende (Cosenza), Italy*
[b] *Department of Engineering and Architecture, University of Parma, Parco Area delle Scienze 181/A, I-43100 Parma, Italy*
[c] *Construction Technologies Institute - Italian National Research Council (ITC-CNR), Via Lombardia 49, I-20098 San Giuliano Milanese (Milano), Italy*

Abstract

Solid-shell models are developed for the geometrically nonlinear analysis of multi-layered composite structures made of alternating layers with large difference in material properties. Exemplificative applications are presented for laminated glass, in which a number of stiff plies of glass are permanently shear-coupled by soft interlayers. The sectional warping due to significant transverse shear strains in the soft layers makes theories of laminated plates based on the plane-section hypothesis unreliable. The proposed approach is based on a geometrically exact solid-shell finite element model with one element per layer in the thickness direction, as alternative to solid discretization. The element approximation is based on the displacement nodal values at the top and bottom surfaces of the layers, with a natural C^0 continuity. An alternative solid-shell model with fewer parameters is derived imposing the equal finite rotation of the stiff layers at each surface point by a local rotation-free re-parametrization of the nodal displacements and enforcing the plane stress condition. The approach permits an easy coupling with a fully solid discretization, e.g. to model connections, and is based on a simple strain measure quadratic in the displacement unknowns and suitable for finite strains. Extensive numerical examples for laminated glass plates and curved shells susceptible to large deflections and buckling are provided, comparing the results with those from a fully solid approach.

Keywords: Layered structures, laminated glass, solid-shell model, finite element method, buckling, geometric nonlinearity.

1. Introduction

Laminated structures are made of different adherent layers, or of layers of the same anisotropic material but with different orientation as in fiber-reinforced composites. A particular class is represented by laminates formed by the alternating association of layers made of stiff and soft materials, for which the drastic change in mechanical properties induces an irregular warping of the cross sections. This is why homogenized models, such as the first or higher order theory of laminated plates, are in general not sufficient to capture the structural response in terms of deflections, stress and buckling. A solid continuum model could capture the local and global effects, but the 3D finite element discretization usually requires a huge computational cost. Therefore, a significant effort has been developed in the last decades to conceive enriched plate theories for laminates with an improved estimation of the peculiar kinematics at reduced computational burden. Layer-wise models [1, 2, 3] and zigzag models [4, 5, 6] achieve the representation of a piecewise continuous

*Corresponding author
Email addresses: domenico.magisano@unical.it (Domenico Magisano), leonardo.leonetti@unical.it (Leonardo Leonetti), giovanni.garcea@unical.it (Giovanni Garcea), gianni.royer@unipr.it (Gianni Royer-Carfagni)

displacement in the thickness direction by employing the first order, or higher order, shear deformation theories *at each layer* and imposing continuity conditions at the interfaces. In general, the accuracy of a model for thin-to-moderately-thick plates depends significantly on the ability to capture the zigzag effect, whereas its efficiency is a function of the number of independent displacement variables as well as of the sparsity of the resulting equations. Here, we propose a solid-shell model for the geometric nonlinear analysis of laminates with alternating stiff/soft layers, for which a simplified (constrained) kinematic description facilitates the finite element computation.

A paradigmatic example of composites with alternating stiff/soft stacking sequence is represented by laminated glass. This is made by two (or more) glass plies permanently bonded by one (or more) polymeric interlayers, thanks to the chemical affinity developed in a process at high temperature and pressure in autoclave. There are many types of carbon-based polymeric films [7]. The most used are the polyvinyl butyral (PVB), the ionoplast SentryGlas (SG) and the ethylene-vinyl acetate (EVA). More recently, transparent silicone polymers, specifically produced to form interlayers, have been commercialized [8].

Although polymers are in general highly viscoelastic [9], a widely-used engineering approach is the *quasi-elastic approximation* [10]: the polymer is modelled as a linear elastic material but with temperature- and time-dependent stiffness, coinciding with the secant value measured in relaxation tests at operating temperature, after a time corresponding to the duration of the design loads. The corresponding elastic modulus is variable within the order of 0.1 MPa for the softer PVB at 40°C under permanent loads (20 years duration), and of 100 MPa for the stiffer SG at 0°C under short-term (3 s) actions. The viscosity of silicone is much smaller than that of carbon polymers: the Young's modulus, of the order of 5 MPa, remains stable within a wide temperature range, rendering silicone interlayers particularly suitable for extreme applications. Anyway, in all the aforementioned cases, the stiffness of the interlayers is several orders of magnitude lower than that of glass, whose Young's modulus is approximately 70 GPa.

In architectural and automotive applications, the thickness of the glass plies may vary within $1-19$ mm, whereas that of the polymeric interlayers is in general a multiple of 0.38 mm, up to about 2.28 mm, but can be higher for silicone. Although the interlayer film has in practice no bending stiffness by itself, it can restrain the shear-sliding of the glass plies. This increases the overall bending capacity of the laminate, which varies [11] between the lower bound of free-sliding glass plies (*layered limit*) and the opposite upper-bound of perfectly coupled glass plies (monolithic limit). Correspondingly, the irregular character of the cross-sectional warping is maximal at the layered limit and minimal (no warping) at the monolithic limit.

However, technological progress and new manufacturing techniques make innovative materials available on a large scale, or furnish traditional materials with exceptional shapes and sizes. As for glass, there have been many innovations but two trends are worth mentioning here. On the one hand, the available size of the plates has increased: lengths of the order of 20 m have been reached. On the other hand, it is nowadays possible to produce long glass plates of width of the order of 1.2 m with very small thickness, down to 0.5 mm; but ultra-thin glass could also be produced, down to 50 μm. Thin glass, whose mechanical strength is enhanced [12] in a toughening process by ion exchange, has been used for years in portable electronic device displays: the increase in size makes it possible to produce large laminates made up of a considerable number of plies, achieving remarkable properties in terms of toughness and impact resistance, including bullet penetration. But transparent layers can also be made with plastic materials, such as Polymethyl methacrylate (PMMA) [13], also known as acrylic glass, or polycarbonate [14], a thermoplastic polymer containing carbonate groups. Materials of this type are often referred to [15] as "plastic glass". Although their mechanical stiffness and strength are lower than that of glass, they are used in aircraft, automotive and security components, because they are not as brittle as glass, at least as long as the temperature is not extremely low. Glass and plastic glass of different thicknesses may be combined together [16] in transparent laminates with functionally graded properties. However, since the coefficient of thermal expansion of glass (of the order of $10^{-5}\,\mathrm{K}^{-1}$ for soda-lime glass) is very different from that of plastic glass (of the order of $10^{-4}\,\mathrm{K}^{-1}$), very compliant interlayers are needed to accommodate the thermal mismatch.

The category of laminated glass should be therefore generalized to the broader concept of *transparent composite*, where a number of stiff, possibly curved, plies of large size, with different thicknesses and mechanical properties, are coupled through very soft thin interlayers. The alternating layup induces a specific straining/deformation pattern, which distinguishes them from other composites [17, 18]. In fact, the trans-

verse shear strains tend to concentrate in the soft interlayers, with a nearly constant distribution in the thickness, while they are negligible in the stiff plies. Moreover, although the interlayers are soft, their moderate thickness and the confining action of the neighboring bonded layers is such as to constrain the relative distance between the surfaces to which they adhere. The consequence is that the stiff layers are all subjected to almost identical rotations with respect with their normals in the undistorted configuration, while the soft layers undergo independent transverse shear strains. A geometric-nonliner model is in general required, because the slenderness of the structure and the compliance of the interlayers provide large deflections.

Different plate/shell models have been proposed for alternating layups. A software specific for laminated glass which has been broadly used in the design practice for the last two decades, is SJ MEPLA. The theory followed for its implementation [19] consists in the discretization into Mindlin-Reissner finite elements of each stiff layer, with independent rotations and in-plane displacements. The transverse displacement is assumed equal for all the layers and the kinematics of the soft layers is derived from the stiff layers variables, assuming perfect bonding and negligible thickness strain. There are, however, the following limitations: only flat geometries are allowed; the model is not exact for large deformations (second-order accuracy only); the nonlinear solver is only load-controlled and, hence, not suitable for general instability problems. A significant step forward was given in [17] where, for the first time, a shell model imposing equal rotation of the stiff layers and independent slips of the soft interlayers was proposed. This is a Mindlin-Reissner model enriched by independent in-plane displacements of the soft layers, for which the equal rotation of the stiff layers is a direct variable. The same work provides a locking-free shell finite element and the geometrically nonlinear model is recovered by the co-rotational strategy, suitable for small strain problems [20]. Further developments are reported in [21], in particular for what concerns the modeling of creep in the viscoelastic interlayers. Most often, the stiff layers tend to exhibit negligible transverse shear strains. Although limited to small-displacement analyses, the Kirchhoff assumption of neglecting the transverse shear strains in the stiff layers was exploited in [18], with the aim of further reducing the model variables. However, the weak form of the Kirchhoff model requires at least C^1 continuity, which can be met only with special finite element formulations or isogeometric analyses [22, 23, 24].

Besides the Kirchhoff and Reissner models, it is worth mentioning alternative formulations for modeling shells in large deformations such as the solid-shell approach [25, 26, 27, 28]. This modeling strategy is based on a 3D continuum model with an assigned kinematic approximation in the thickness direction obtained directly in the discrete model. The goal is to maintain a solid description of geometry and kinematics and, at the same time, to reduce the number of unknowns with respect to a fully solid model in order to obtain a discretization based on a similar number DOFs compared to the Reissner shell model. The advantages with respect to a Reissner shell model are multiple: solid modeling of intersections, constraints and contact, Total Lagrangian kinematic description in terms of displacement DOFs only (no finite rotation parameterizations and their complications [29, 30, 31]) with a quadratic Green-Lagrange strain measure and an easy coupling with solids. For laminates, homogenized solid-shell models equivalent to the first order shear deformation theory have been proposed [25], while in other works, e.g. in [32], it is also stated the possibility of using effectively one element per layer, when needed.

This latter approach is the starting point of the present work, aimed at providing an efficient solid-shell formulation for the geometrically nonlinear analysis of multi-layered composite structures made of alternating stiff/soft layers. Applications are to laminated glass or, more in general, to transparent composites. The basic constituent is a geometrically-exact solid-shell finite-element model, with one element in the thickness direction per layer, as an alternative to a 3D solid discretization. The element approximation is based on the displacement nodal values at top and bottom surfaces of the layers with a direct imposition of the C^0 continuity in the assembly procedure. The finite element formulation is purely displacement-based and locking-free without internal parameters thanks to the plane stress enforcement. From this, a novel solid-shell model with fewer parameters is derived by exploiting the main feature of the considered problem, i.e., by imposing an equal finite rotation of the stiff layer elements at each surface point. Such a kinematic constraint is applied directly to the discrete model by a local rotation-free re-parametrization of the nodal displacements and enforcing the plane stress condition. It is worth noting that, in this Total Lagrangian model, the strain measure is accurate and geometrical exact for any mesh and with no assumption on the strain magnitude, as opposite to co-rotational shell formulations. With respect to the enriched Reissner

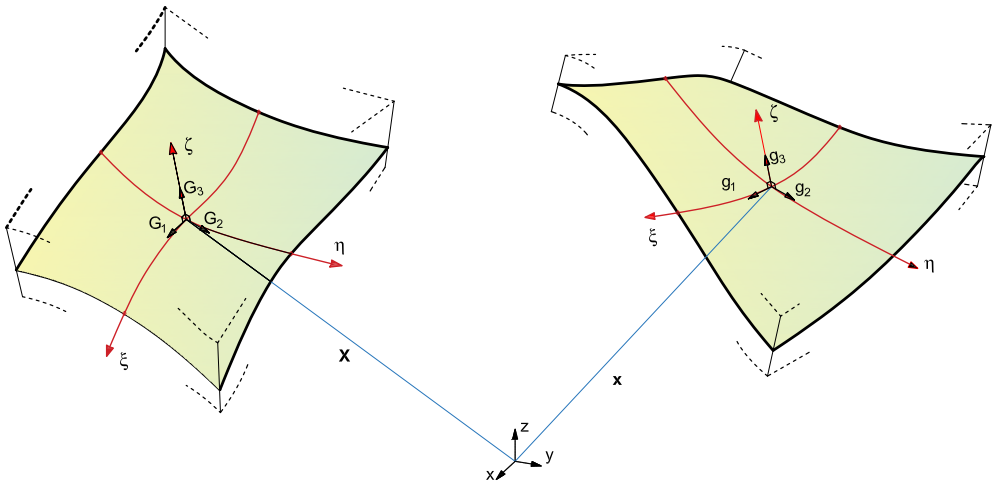

Figure 1: Undeformed and deformed shell geometry.

shell model in [17], the overall number of DOFs is just a little higher due to the possible thickness change, but with a more computationally efficient evaluation of the discrete quantities due to the simpler expression of the strain and of its variations with no co-rotational transformations. Moreover, the constraint of equal finite rotation of the stiff layer is local at each surface point and can be deactivated, when needed, to model connections and 3D stress concentrations by a coupling with a fully solid discretization [33].

The article is organized as follows. In Section 2 the solid-shell model is present in a Total Lagrangian description. The finite element implementation for laminates with assumed natural strain is reported in Section 3. Extensive numerical results on laminated glass plates and curved shells, amenable of large deflections and buckling, are provided in Section 4, comparing the constrained solid-shell model with the layer-wise solid-shell and the fully solid solution from Abaqus. The main advantages of the proposed formulation, its limitations and hints for further work are summarized in the conclusive Section 5.

2. Solid-shell model

This section describes the main equations of the solid-shell model initially proposed in [25] and presented here in a Total Lagrangian description with a Green-Lagrange strain measure. The starting point is a 3D finite kinematics of each layer in terms of displacement only. Then, a linear through-the-thickness approximation is assumed for geometry and displacement. Generalized strains and the generalized constitutive matrix are derived.

2.1. Kinematics and strain measure for each layer

Convective curvilinear shell coordinates $\boldsymbol{\xi} = [\xi, \eta, \zeta]$ are employed, with (ξ, η) middle surface coordinates and $\zeta \in [-\frac{h}{2}, \frac{h}{2}]$ thickness coordinate and h the layer thickness. The position of the material points $\mathbf{x}[\boldsymbol{\xi}]$ in the current configuration is given in terms of their position vector $\mathbf{X}[\boldsymbol{\xi}]$ in the reference configuration and the displacement $\mathbf{d}[\boldsymbol{\xi}]$

$$\mathbf{x}[\boldsymbol{\xi}] = \mathbf{X}[\boldsymbol{\xi}] + \mathbf{d}[\boldsymbol{\xi}]. \tag{1}$$

The covariant basis vectors in the undeformed configuration are obtained from the corresponding partial derivatives $\mathbf{G}_i = \mathbf{X}_{,i}$ of the position vectors $\mathbf{X}$, where $()_{,i}$ denotes the partial derivative with respect to the ith component of $\boldsymbol{\xi}$. Letting $\mathbf{G}^i$ the contravariant basis so that $\mathbf{G}^i \cdot \mathbf{G}_j = \delta_{ij}$ with δ_{ij} the Kronecker delta and $(\cdot)$ denoting scalar product, the Green-Lagrange strain tensor can be expressed as

$$\mathbf{E}_{GL} = \bar{E}_{ij}\, \mathbf{G}^i \otimes \mathbf{G}^j, \quad \bar{E}_{ij} = \frac{1}{2}\left(\mathbf{X}_{,i} \cdot \mathbf{d}_{,j} + \mathbf{d}_{,i} \cdot \mathbf{X}_{,j} + \mathbf{d}_{,i} \cdot \mathbf{d}_{,j}\right), \quad i,j = 1,2,3. \tag{2}$$

where $(\otimes)$ indicates the tensor product.

Assuming a linear through-the-thickness approximation, the position vector is expressed as

$$\mathbf{X} = (\frac{1}{2} - \frac{\zeta}{h})\mathbf{X}_b[\xi,\eta] + (\frac{1}{2} + \frac{\zeta}{h})\mathbf{X}_t[\xi,\eta] \tag{3}$$

in terms of the bottom and top position of the shell/layer

$$\mathbf{X}_b[\xi,\eta] = \mathbf{X}[\xi,\eta,-\frac{h}{2}], \qquad \mathbf{X}_t[\xi,\eta] = \mathbf{X}[\xi,\eta,\frac{h}{2}].$$

Similarly, the displacement field is approximated as

$$\mathbf{d} = (\frac{1}{2} - \frac{\zeta}{h})\mathbf{d}_b[\xi,\eta] + (\frac{1}{2} + \frac{\zeta}{h})\mathbf{d}_t[\xi,\eta] \tag{4}$$

where

$$\mathbf{d}_b[\xi,\eta] = \mathbf{d}[\xi,\eta,-\frac{h}{2}], \qquad \mathbf{d}_t[\xi,\eta] = \mathbf{d}[\xi,\eta,\frac{h}{2}].$$

By exploiting Eq.(2), the covariant strain components are collected, using a Voigt notation, in the six-dimensional vector $\bar{\mathbf{E}} = [\bar{E}_{11}, \bar{E}_{22}, 2\bar{E}_{12}, \bar{E}_{33}, 2\bar{E}_{23}, 2\bar{E}_{13}]^T$ and linearized with respect to ζ, under the assumption of small layer thickness as compared to the mid-surface dimensions, in the form

$$\bar{\mathbf{E}} \approx \begin{bmatrix} \bar{\mathbf{e}}[\xi,\eta] + \zeta\, \bar{\boldsymbol{\chi}}[\xi,\eta] \\ \bar{E}_{33}[\xi,\eta,0] \\ \bar{\boldsymbol{\gamma}}[\xi,\eta] \end{bmatrix} \tag{5}$$

where

$$\bar{\mathbf{e}}[\xi,\eta] = \begin{bmatrix} \bar{E}_{11}[\xi,\eta,0] \\ \bar{E}_{22}[\xi,\eta,0] \\ 2\bar{E}_{12}[\xi,\eta,0] \end{bmatrix}, \quad \bar{\boldsymbol{\chi}}[\xi,\eta] = \begin{bmatrix} \bar{E}_{11,3}[\xi,\eta,0] \\ \bar{E}_{22,3}[\xi,\eta,0] \\ 2\bar{E}_{12,3}[\xi,\eta,0] \end{bmatrix}, \quad \bar{\boldsymbol{\gamma}}[\xi,\eta] = \begin{bmatrix} 2\bar{E}_{23}[\xi,\eta,0] \\ 2\bar{E}_{13}[\xi,\eta,0] \end{bmatrix}.$$

It is worth noting that such a linearization with respect to the thickness coordinate does not imply any assumptions on displacement and strain magnitude. From the point of view of theoretical modelling, it is definitively not necessary; however, it is very convenient for an efficient analytical pre-integration through the thickness, as detailed in Section 2.1.1. A Cartesian reference system is defined at each point $\mathbf{X}$ by the orthonormal basis $\{\mathbf{e}_1, \mathbf{e}_2, \mathbf{e}_3\}$ with $\mathbf{e}_3$ aligned with $\mathbf{G}_3$ and $\{\mathbf{e}_1, \mathbf{e}_2\}$ in the shell middle surface. The generalized Cartesian strains are obtained from the covariant ones as

$$\boldsymbol{\varepsilon} = \mathbf{T}[\xi,\eta]\bar{\boldsymbol{\varepsilon}} \quad \text{with} \quad \boldsymbol{\varepsilon} = \begin{bmatrix} \mathbf{e} \\ e_{33} \\ \boldsymbol{\gamma} \\ \boldsymbol{\chi} \end{bmatrix} \quad \text{and} \quad \bar{\boldsymbol{\varepsilon}} = \begin{bmatrix} \bar{\mathbf{e}} \\ \bar{e}_{33} \\ \bar{\boldsymbol{\gamma}} \\ \bar{\boldsymbol{\chi}} \end{bmatrix}, \tag{6}$$

where $\bar{e}_{33} = \bar{E}_{33}[\xi,\eta,0]$ and $\mathbf{T}(\xi,\eta)$ denotes the transformation matrix that maps the strain tensor from the covariant basis to the local Cartesian basis according to Eq. (2), i.e.,

$$\mathbf{T}(\xi,\eta) = \begin{bmatrix} \mathbf{T}_p & 0 & 0 & 0 \\ 0 & T_z & 0 & 0 \\ 0 & 0 & \mathbf{T}_p & 0 \\ 0 & 0 & 0 & \mathbf{T}_t \end{bmatrix}, \tag{7}$$

where the sub-matrices

$$\begin{aligned} T_z &= 1/J_{33}^2\,, \\ \mathbf{T}_p &= \begin{bmatrix} J_{11}^2 & J_{12}^2 & 2J_{11}J_{12} \\ J_{21}^2 & J_{22}^2 & 2J_{21}J_{22} \\ J_{21}J_{11} & J_{22}J_{12} & J_{22}J_{11} + J_{21}J_{12} \end{bmatrix}^{-T}, \\ \mathbf{T}_t &= \begin{bmatrix} J_{12}J_{33} + J_{13}J_{32} & J_{13}J_{31} + J_{11}J_{33} \\ J_{22}J_{33} + J_{23}J_{32} & J_{23}J_{31} + J_{21}J_{33} \end{bmatrix}^{-T}, \end{aligned} \tag{8}$$

are obtained from the components of the Jacobian matrix $\mathbf{J}(\xi,\eta,\zeta) = [\mathbf{G}_1,\ \mathbf{G}_2,\ \mathbf{G}_3]^T$.

In Eq.(6) $\mathbf{e}$ is the membrane strain vector, $\boldsymbol{\chi}$ the curvature vector, $\boldsymbol{\gamma}$ the transverse shear strains vector and e_{33} the thickness strain.

It is worth noting that in this solid-shell model the generalized strains have the same form as in the Mindlin-Reissner shear deformable shell model with the additional thickness strain e_{33}. The main advantage is that the kinematics is described in terms of displacement variables only, without the need for a direct parameterization of 3D finite rotations. Indeed, according to Eq. (2), the generalized strains are a quadratic function of $\mathbf{d}$, parametrized in terms of bottom surface field $\mathbf{d}_b$ and top surface field $\mathbf{d}_t$ as stated in Eq. (4).

2.1.1. Strain energy and constitutive matrix of the layer in generalized quantities

The Cartesian components of the Green-Lagrange strain and the second Piola-Kirchhoff stress are collected in vectors $\mathbf{E} = [E_{11}, E_{22}, 2E_{12}, E_{33}, 2E_{23}, 2E_{13}]^T$ and $\mathbf{S} = [S_{11}, S_{22}, S_{12}, S_{33}, S_{23}, S_{13}]^T$, respectively, adopting a Voigt notation. The linear elastic constitutive law can be expressed as

$$\mathbf{S} = \mathbf{C}\mathbf{E} \quad \text{with} \quad \mathbf{C} = \begin{bmatrix} \mathbf{C}_p & \mathbf{0} & \mathbf{0} \\ \mathbf{0} & C_{33} & \mathbf{0} \\ \mathbf{0} & \mathbf{0} & \mathbf{C}_t \end{bmatrix}, \tag{9}$$

where $\mathbf{C}_p$ is obtained by assuming a plane stress condition, while the coupling between membrane and thickness strains is neglected in order to eliminate a-priori the thickness locking. The coefficient C_{33}, linking thickness stress to thickness strain, is maintained in order to avoid a zero energy thickness stretch. The strain energy of the solid-shell model can be conveniently written in terms of generalized strains as

$$\Phi[\mathbf{d}] \equiv \frac{1}{2}\int_\Omega \int_{-\frac{h}{2}}^{\frac{h}{2}} \mathbf{E}[\mathbf{d}]^T \mathbf{C}\mathbf{E}[\mathbf{d}] d\zeta d\Omega = \frac{1}{2}\int_\Omega \boldsymbol{\varepsilon}[\mathbf{d}]^T \boldsymbol{\mathcal{C}} \boldsymbol{\varepsilon}[\mathbf{d}] d\Omega\,, \tag{10}$$

with

$$\boldsymbol{\mathcal{C}} = \begin{bmatrix} \boldsymbol{\mathcal{C}}_{ee} & 0 & \mathbf{0} & \boldsymbol{\mathcal{C}}_{e\chi} \\ 0 & \mathcal{C}_{33} & \mathbf{0} & \mathbf{0} \\ 0 & \mathbf{0} & \boldsymbol{\mathcal{C}}_t & \mathbf{0} \\ \boldsymbol{\mathcal{C}}_{e\chi}^T & \mathbf{0} & \mathbf{0} & \boldsymbol{\mathcal{C}}_{\chi\chi} \end{bmatrix}, \tag{11}$$

where

$$\mathcal{C}_{33} = \int_{-\frac{h}{2}}^{\frac{h}{2}} C_{33} d\zeta \qquad \boldsymbol{\mathcal{C}}_t = \int_{-\frac{h}{2}}^{\frac{h}{2}} \mathbf{C}_t d\zeta\,,$$

$$\boldsymbol{\mathcal{C}}_{ee} = \int_{-\frac{h}{2}}^{\frac{h}{2}} \mathbf{C}_p d\zeta \qquad \boldsymbol{\mathcal{C}}_{e\chi} = \int_{-\frac{h}{2}}^{\frac{h}{2}} \zeta \mathbf{C}_p d\zeta \qquad \boldsymbol{\mathcal{C}}_{\chi\chi} = \int_{-\frac{h}{2}}^{\frac{h}{2}} \zeta^2 \mathbf{C}_p d\zeta\,.$$

The transverse shear stiffness $\boldsymbol{\mathcal{C}}_t$ can be improved by means of shear correction factors.

3. Finite element models for laminates with alternating stiff/soft layup

The FEM implementation of the solid-shell model is now detailed.

3.1. Linear solid-shell finite element with Assumed Natural Strain

The displacement field $\mathbf{d}_b[\xi,\eta]$ and $\mathbf{d}_t[\xi,\eta]$ of bottom and top surfaces of the layer, defining the overall displacement field $\mathbf{d}[\boldsymbol{\xi}]$ in the shell volume according to Eq. (4), can be interpolated, so obtaining

$$\mathbf{d}[\boldsymbol{\xi}] = \mathbf{N}_d[\boldsymbol{\xi}]\mathbf{q}_e \quad \text{with} \quad \mathbf{N}_d[\boldsymbol{\xi}] = \left[(\tfrac{1}{2} - \tfrac{\zeta}{h})\mathbf{N}[\xi,\eta] \quad (\tfrac{1}{2} + \tfrac{\zeta}{h})\mathbf{N}[\xi,\eta]\,,\right] \tag{12}$$

where $\mathbf{q}_e$ collects the element nodal displacement DOFs for both $\mathbf{d}_b$ and $\mathbf{d}_t$, while $\mathbf{N}[\xi,\eta]$ collects the bilinear Lagrangian functions with $\xi \in [-1,1]$ and $\eta \in [-1,1]$. The element geometry is interpolated with the same shape functions according to the isoparametric paradigm

$$\mathbf{X}[\boldsymbol{\xi}] = \mathbf{N}_d[\boldsymbol{\xi}]\mathbf{X}_e\,,$$

where $\mathbf{X}_e$ collects the element nodal positions.

The linear element so defined is prone to transverse shear and trapezoidal locking. However, these inaccuracies can be eliminated very easily by the Assumed Natural Strain (ANS) technique [34], that redefines the transverse shear strain components $\bar{E}_{23}, \bar{E}_{13}$ and the transverse normal strain component $\bar{E}_{33}$ using their values at the sampling points reported in [25]. Moreover, the in-plane bending response of the element can be also enhanced by replacing the in-plane shear strain $\bar{E}_{12}$ with its value at the element center $\xi = \eta = 0$, that is a selective reduced integration (SRI) retaining the correct matrix rank. Finally, the discrete generalized strain-displacement law, omitting the dependence on (ξ, η), can be written in compact form as

$$\boldsymbol{\varepsilon} = (\boldsymbol{\mathcal{L}} + \frac{1}{2}\boldsymbol{\mathcal{Q}}[\mathbf{q}_e])\mathbf{q}_e \,, \tag{13}$$

where $\boldsymbol{\mathcal{L}}$ and $\boldsymbol{\mathcal{Q}}[\mathbf{q}_e]$ are the operators giving the linear and quadratic part of the strain. In particular, matrix $\boldsymbol{\mathcal{L}}$ is constant with respect to $\mathbf{q}_e$, while $\boldsymbol{\mathcal{Q}}$ is a linear function of $\mathbf{q}_e$:

$$\boldsymbol{\mathcal{Q}}[\mathbf{q}_e] \equiv \begin{bmatrix} \mathbf{q}_e^T \boldsymbol{\Psi}_1 \\ \vdots \\ \mathbf{q}_e^T \boldsymbol{\Psi}_9 \end{bmatrix} \quad \text{and} \quad \boldsymbol{\mathcal{L}} = \boldsymbol{\mathcal{Q}}[\mathbf{X}_e].$$

The explicit expression of the matrices $\boldsymbol{\Psi}_i$ can be easily obtained from Eq. (5) and (6) (see [35]). Clearly, $\boldsymbol{\mathcal{L}}$ and $\boldsymbol{\mathcal{Q}}$ depend on the mid-surface coordinates (ξ, η), but this is omitted from now on to simplify the notation. The strain energy of the structure can be evaluated as a sum of element contributions Φ_e computed by a 2×2 Gauss quadrature, i.e.,

$$\Phi_e[\mathbf{q}_e] \equiv \frac{1}{2} \sum_g \left\{ \boldsymbol{\varepsilon}_g[\mathbf{q}_e]^T \boldsymbol{\mathcal{C}} \boldsymbol{\varepsilon}_g[\mathbf{q}_e] \right\} w_g \,, \tag{14}$$

where the subscript g denoted quantities at the generic integration point (ξ_g, η_g) and w_g is the corresponding weight times the determinant of the Jacobian matrix.

3.2. Remarks on thickness locking

In Eq. (9), the 3D constitutive law was simplified using the plane stress enforcement (PSE) to avoid the thickness locking arising from the assumption of linear displacement through the thickness. Alternative strategies based on the exact 3D constitutive behavior are possible:

- modified generalized constitutive matrix (MGCM);
- mixed formulation (MF);
- enhanced assumed strain (EAS).

MGCM [25] starts from the full 3D constitutive matrix of the continuum problem and derives the constitutive matrix in generalized quantities from Eq. (10), by imposing a constant thickness stress S_{33} in the through-the-thickness analytical integration instead of a constant thickness strain E_{33}. This results in a thickness locking-free displacement-based formulation without the need for additional variables.

Similarly, the MF is based on an independent approximation of the stress with S_{33}, assumed constant through the thickness within the Hellinger-Reissner principle [36]. The difference with the MGCM is that additional variables for the stress are introduced. However, the stress field is discontinuous across elements and this means that the corresponding variables can be condensed out before solving the global linear systems (Newton iterations at each equilibrium point).

Another popular technique is EAS, that enhances the thickness strain with an incompatible part variable in the thickness direction. As in the MF, also EAS introduces additional variables that can be condensed out at element level and is particularly convenient for 3D nonlinear constitutive laws [34].

3.3. Layered solid-shell modeling for generic laminates

Generic laminated structures are made of multiple layers with different material properties. When these change significantly through the plate thickness, the deformation is characterized by zigzag forms of the displacement field along the thickness direction. This significant warping makes homogenized models, such as the first order theory of laminated plates, not sufficient to capture the structural response accurately. Solid models can be used to obtain a reliable solution by discretizing the structure also through the thickness. However, general purpose solid finite elements are not suitable for layered plates, because they require either to mesh also within each layer, or to use high order interpolations. For this reason, a layered solid-shell model, i.e., with a single solid-shell element per layer, is an interesting alternative. In this case, the total number of variables at each point over the surface of the plate is $n_t = 3(n_l + 1)$, taking into account the continuity of the displacement among the n_l layers. All the approaches for removing thickness locking, i.e. PSE, MGCM, MF and EAS, can be adopted in such a modeling. It is worth noting that, as opposite to corotational shell models, no restriction in the magnitude of transverse shear strains of the soft layers is assumed in the kinematic model.

3.4. A solid-shell model for laminates with alternating stiff/soft layup

A special group of laminates is that characterized by alternating stiff/soft layers with a large change in the material properties. Focusing on structural glass laminates, the stiff parts are glass layers, while the soft parts are usually made of thermoplastic polymers or silicone. The Young and shear modulus of the two material types differ of many orders of magnitude. The alternating layup induces a specific deformation pattern with all stiff layers exhibiting an almost identical rotation of their respective initial normals, whereas the soft layers can have different rotations as a consequence of the significant and independent transverse shear strains. A specialized solid-shell modeling strategy is now presented for laminates with alternating stiff/soft layup by constraining all the stiff layers to maintain the same orientation during the deformation. In this case, the total number of variables is reduced to $n_t = 3(n_l + 3)/2$, with odd n_l, by a simple linear combination of the discrete displacement parameters, as illustrated in Fig. 2. In this figure, $\mathbf{q}_i$ with $i = 1 \dots n_l + 1$ collects the 3 displacement components of the FE nodes at a generic point of the plate. These can be written in terms of a reduced number of parameters by a constant transformation matrix that is reported explicitly, as an example, in Eq. (15) and Eq. (16) for the case $n_l = 3$ and $n_l = 5$ respectively. Clearly, the reduction is possible for any odd number of layers, with the transformation matrix that follows the same rule. The reduced variables are $\mathbf{q}_n$ and $\mathbf{q}_{ij}$. Vector $(\mathbf{q}_j - \mathbf{q}_i)/h_{ij}$, defining the rotation of the initial normal of the generic stiff layer delimited by nodes i and j, with h_{ij} the thickness of the layer, is constrained as $(\mathbf{q}_j - \mathbf{q}_i)/h_{ij} = \mathbf{q}_n$, with $\mathbf{q}_n$ the same for all the stiff layers. Instead, $\mathbf{q}_{ij} = (\mathbf{q}_i + \mathbf{q}_j)/2$ is the independent mean displacement of each stiff layer.

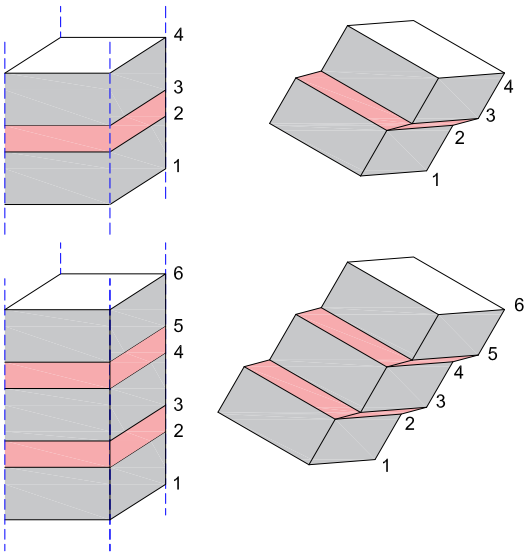

$$\begin{bmatrix}\mathbf{q}_1\\ \mathbf{q}_2\\ \mathbf{q}_3\\ \mathbf{q}_4\end{bmatrix} = \begin{bmatrix}1 & 0 & -\frac{h_{12}}{2}\\ 1 & 0 & \frac{h_{12}}{2}\\ 0 & 1 & -\frac{h_{34}}{2}\\ 0 & 1 & \frac{h_{34}}{2}\end{bmatrix} \begin{bmatrix}\mathbf{q}_{12}\\ \mathbf{q}_{34}\\ \mathbf{q}_n\end{bmatrix} \tag{15}$$

$$\begin{bmatrix}\mathbf{q}_1\\ \mathbf{q}_2\\ \mathbf{q}_3\\ \mathbf{q}_4\\ \mathbf{q}_5\\ \mathbf{q}_6\end{bmatrix} = \begin{bmatrix}1 & 0 & 0 & -\frac{h_{12}}{2}\\ 1 & 0 & 0 & \frac{h_{12}}{2}\\ 0 & 1 & 0 & -\frac{h_{34}}{2}\\ 0 & 1 & 0 & \frac{h_{34}}{2}\\ 0 & 0 & 1 & -\frac{h_{56}}{2}\\ 0 & 0 & 1 & \frac{h_{56}}{2}\end{bmatrix} \begin{bmatrix}\mathbf{q}_{12}\\ \mathbf{q}_{34}\\ \mathbf{q}_{56}\\ \mathbf{q}_n\end{bmatrix} \tag{16}$$

Figure 2: Constrained kinematics of laminates with alternating stiff/soft layers.

It is important to note that only the PSE can be adopted in this modeling among the different strategies for avoiding thickness locking. In fact, MGCM, MF and EAS, all based of the full 3D constitutive law, removes thickness locking but lead to an undesirable effect when an equal vector $\mathbf{q}_n$ is imposed. This is due to the fact that such a constraint not only states the desired equal orientation of the stiff layers, but also an equal norm of such a vector. This means that the stiff layers cannot have different changes in the thickness length (thickness strain). In such a kinematic condition, an additional Poisson locking occurs if a full 3D constitutive law is used, that is instead avoided if the PSE is considered.

With respect to co-rotational shell models, this solid-shell modeling with equal orientation of the stiff layers requires no assumptions on the strain magnitude and uses a geometrically exact strain measure for any mesh. Also, it maintains the solid description and the rotational constraint can be deactivated, when needed, to model connections and 3D stress concentrations by a direct coupling with a fully solid discretization.

3.5. Equilibrium path and Riks method

Let us consider a slender hyperelastic structure subject to a conservative reference load vector $\mathbf{p}$ proportionally increased by an amplifier factor λ. The strain energy of the whole structure is the sum of all element contributions

$$\Phi[\mathbf{q}] \equiv \sum_e \Phi_e[\mathbf{q}_e]\,, \tag{17}$$

where $\mathbf{q}$ collects all the displacement DOFs of the FE mesh. The equilibrium of the structure is expressed by the virtual work equation in discrete form

$$\mathbf{r}[\mathbf{q}] \equiv \mathbf{s}[\mathbf{q}] - \lambda\mathbf{p} = \mathbf{0}\,. \tag{18}$$

The internal force vector $\mathbf{s}$ is defined as

$$\mathbf{s}[\mathbf{q}] \equiv \frac{\partial\Phi[\mathbf{q}]}{\partial\mathbf{q}}\,, \tag{19}$$

and it can be then evaluated by assembling its element contributions

$$\mathbf{s}_e[\mathbf{q}] = \sum_g \left\{\boldsymbol{\mathcal{B}}_g[\mathbf{q}_e]^T\boldsymbol{\mathcal{C}}\boldsymbol{\varepsilon}_g[\mathbf{q}_e]\right\} w_g\,, \tag{20}$$

with $\boldsymbol{\mathcal{B}}[\mathbf{q}_e] = \boldsymbol{\mathcal{L}} + \boldsymbol{\mathcal{Q}}[\mathbf{q}_e]$. Eq. (18) is a system of N equations in $N+1$ unknowns, i.e. $\{\mathbf{q}, \lambda\}$, defining the equilibrium path as a curve in $\mathbb{R}^{N+1}$. The standard approach for tracing this curve in stability problems is the Riks arc-length method due to its ability to deal with limit points. The path is evaluated starting from a known initial configuration $\mathbf{u}_0$ corresponding to $\lambda = 0$ in an incremental-iterative manner. In practice, at each step, a new equilibrium point is obtained by solving an extended system

$$\mathbf{R}[\mathbf{q}, \lambda] \equiv \begin{bmatrix} \mathbf{r} \\ g \end{bmatrix} = \begin{bmatrix} \mathbf{s}[\mathbf{q}] - \lambda \mathbf{p} \\ \Delta\mathbf{q}_0^T \Delta\mathbf{q} + \mu \Delta\lambda_0 \Delta\lambda - \Delta s \end{bmatrix} = \mathbf{0}\,, \tag{21}$$

where the equation $g = 0$ is an arc-length constraint, $\Delta s \geq 0$ defines the step size, $\Delta\mathbf{q}_0$ and $\Delta\lambda_0$ are estimates of the current path tangent and μ is a metric factor to homogenize the different quantities. The solution of (21) can be obtained by a Newton iterative scheme in partitioned form

$$\begin{cases} \mathbf{q}_{j+1} = \mathbf{q}_j + \dot{\mathbf{q}}_j \\ \lambda_{j+1} = \lambda_j + \dot{\lambda}_j \end{cases} \quad \text{with} \quad \begin{cases} \dot{\mathbf{q}} = -\mathbf{K}_j^{-1} \left(\mathbf{r}_j - \dot{\lambda}_j \mathbf{p} \right) \\ \dot{\lambda} = \dfrac{g_j + \Delta\mathbf{q}_0^T \mathbf{K}_j^{-1} \mathbf{r}_j}{\Delta\mathbf{q}_0^T \mathbf{K}_j^{-1} \mathbf{p} - \mu \Delta\lambda_0} \end{cases},$$

in order to exploit the symmetric band structure of the tangent stiffness matrix $\mathbf{K}$ by an $\mathbf{L}^T\mathbf{D}\mathbf{L}$ factorization. This last one is defined as

$$\mathbf{K}[\mathbf{q}] \equiv \frac{\partial^2 \Phi[\mathbf{q}]}{\partial \mathbf{q}^2} \equiv \frac{\partial \mathbf{s}[\mathbf{q}]}{\partial \mathbf{q}}\,, \tag{22}$$

and it can be evaluated by assembling the element contributions

$$\mathbf{K}_e[\mathbf{q}] = \sum_g \left\{ \boldsymbol{\mathcal{B}}_g[\mathbf{q}_e]^T \boldsymbol{\mathcal{C}}_g \boldsymbol{\mathcal{B}}_g[\mathbf{q}_e] + \boldsymbol{\mathcal{G}}_g[\boldsymbol{\sigma}_g] \right\} w_g \quad \text{with} \quad \boldsymbol{\sigma}_g[\mathbf{q}_e] \equiv \boldsymbol{\mathcal{C}}_g \boldsymbol{\varepsilon}_g[\mathbf{q}_e]\,, \tag{23}$$

where $\boldsymbol{\mathcal{G}}[\boldsymbol{\sigma}]$ is the contribution to the geometric part of the stiffness matrix. Exploiting the linear dependence of $\boldsymbol{\mathcal{Q}}[\mathbf{q}_e]$ from $\mathbf{q}_e$ (Eq. (13)) and the symmetry of matrices $\boldsymbol{\Psi}_i$, we have

$$\begin{aligned} \boldsymbol{\mathcal{Q}}[\mathbf{q}_{e1}]\mathbf{q}_{e2} &= \boldsymbol{\mathcal{Q}}[\mathbf{q}_{e2}]\mathbf{q}_{e1}, \quad \forall \mathbf{q}_{e1}, \mathbf{q}_{e2}\,, \\ \boldsymbol{\sigma}^T \boldsymbol{\mathcal{Q}}[\mathbf{q}_e]\mathbf{q}_e &= \mathbf{q}_e^T \boldsymbol{\mathcal{G}}[\boldsymbol{\sigma}]\mathbf{q}_e\,, \end{aligned} \tag{24}$$

where, denoting with σ_i the ith generalized stress $\boldsymbol{\sigma}_g[\mathbf{q}_e]$ component,

$$\boldsymbol{\mathcal{G}}[\boldsymbol{\sigma}] \equiv \sum_i^9 \sigma_i[\xi, \eta] \boldsymbol{\Psi}_i[\xi, \eta].$$

3.5.1. Remarks on the iterative solution for a displacement formulation

The displacement-based path-following analysis is an effective tool for geometrically nonlinear analyses. However, its major drawback is that the iterative solution gets slower and less robust when the slenderness of the structure increases. In particular, when the membrane-to-flexural stiffness ratio gets higher, the allowed load step decreases and more iterations are needed in each step. This is an undesirable behavior due to the use of kinematic variables only as unknowns of the iterative scheme [37, 38]. In that context, the issue can be solved effectively by means of a mixed iteration that relaxes the constitutive law during the iterations using local stress variables at the integration points directly corrected as independent unknowns [37]. This strategy was employed to solve the numerical tests more efficiently.

4. Numerical results

Glass laminated structures undergoing buckling and/or large deflections are analyzed in this section in order to validate and test the proposed solid-shell finite element model. In particular, three modeling are

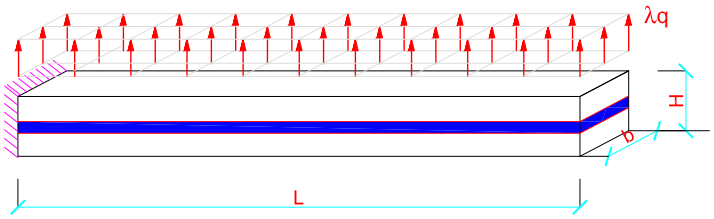

Figure 3: Cantilever beam under transverse load: geometry, load, and boundary conditions.

compared: i) the fully solid model of Abaqus used as a reference solution, ii) the solid-shell model with one element per layer and iii) the solid-shell model where the constraint of equal finite rotation of the stiff layers is applied to reduce the number of unknowns.

Three different layups are used in the numerical tests. For the sake of brevity, they are described only once below.

- Layup $L3_A$: 3 alternating layers of which 2 stiff layers of 4 mm with $E = 70$ GPa and $\nu = 0.23$ and 1 interlayer of 1.02 mm with $E = 1$ MPa and $\nu = 0.49$.
- Layup $L3_B$: 3 alternating layers of which 2 stiff layers of 0.5 mm with $E = 70$ GPa and $\nu = 0.23$ and interlayer of 2.04 mm with $E = 0.2$ MPa and $\nu = 0.49$.
- Layup $L5$: 5 alternating layers of which 3 stiff layers of 12 mm with $E = 70$ GPa and $\nu = 0.23$ and 2 interlayers of 1.52 mm with $E = 5.96$ MPa and $\nu = 0.49$.

Although these packages are purely theoretical, since they only intend to be representative of a sufficiently wide range of geometries and materials, they can be interpreted in the broad category of laminated glass. In all the examples, the elastic parameters of the stiff layers are typical of soda-lime glass, whereas the stiffness of the interlayers may be representative of silicone, PVB and SG, with thickness as measured on some manufactured specimens.

4.1. Large deflection of a 3-layer cantilever beam loaded by a transverse distributed load

The first test regards a cantilever beam of length $L = 500$ mm subject to a distributed transversal load on the top glass layer as illustrated in Fig. 3. The stacking sequences $L3_A$ and $L3_B$ are considered. The reference surface load is $q = 10^{-3}$ MPa for $L3_A$ and $q = 10^{-4}$ MPa for $L3_B$. The solid-shell finite element model consists of 8 elements along the beam axis and only 1 along the width. The load factor vs. tip displacement equilibrium curve is reported in Fig. 4 for the two layups and using the different models. Axial component u and transverse component w are monitored. It is possible to observe an excellent match between solid-shell and constrained solid-shell model up to large deformations. The results are also in agreement with those provided by Abaqus with a fine mesh of solid elements. This is to prove the accuracy of the proposed constrained solid-shell modeling, that uses a reduced number of unknowns but preserves the solid description. The deformed configurations obtained by the unconstrained solid-shell are plotted in Fig. 5, where it is possible to observe the warping of the sections due to the significant shear strain in the interlayer, especially for the layup A, and the equal finite rotation of the glass layers. Finally, the axial normal stress and the transverse shear strain are depicted in Fig. 6 and Fig. 7 for layup $L3_A$ and $L3_B$, respectively, with the thickness dimension amplified to make the through-the-thickness trend visible. We can note that the shear strain is concentrated in the interlayer and is variable with respect to the beam axis due to the end effect of the fully clamped boundary condition. Moreover, the normal stress has a piece-wise linear distribution that is intermediate between the monolithic limit and the layered limit, with independent glass plies, demonstrating the necessity of the proposed kinematic description.

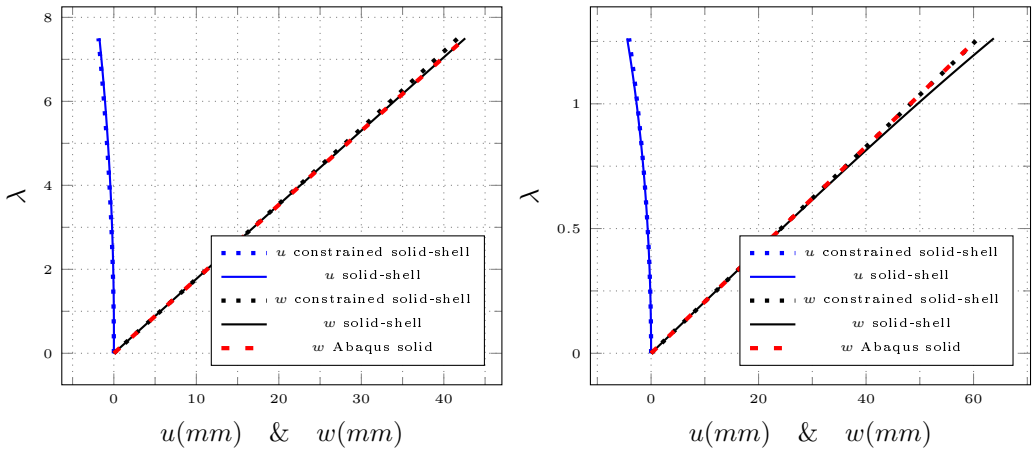

Layup $L3_A$ Layup $L3_B$

Figure 4: Cantilever beam under transverse load: comparison of the equilibrium path obtained by constrained solid-shell and solid-shell model in terms of axial (u) and vertical (w) tip-displacement components and the results from Abaqus.

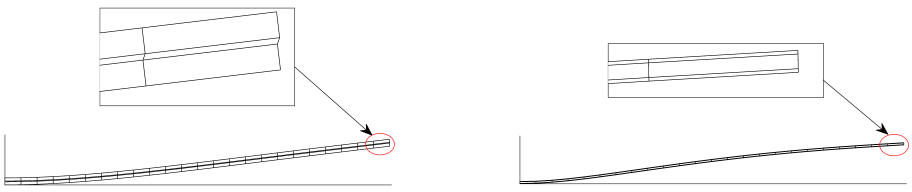

Layup $L3_A$ Layup $L3_B$

Figure 5: Cantilever beam under transverse load: deformed configuration at the last equilibrium point.

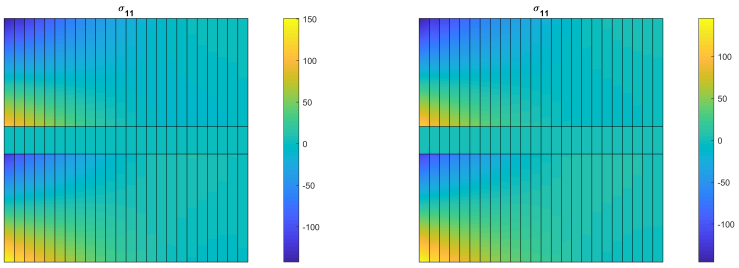

solid-shell constrained solid-shell

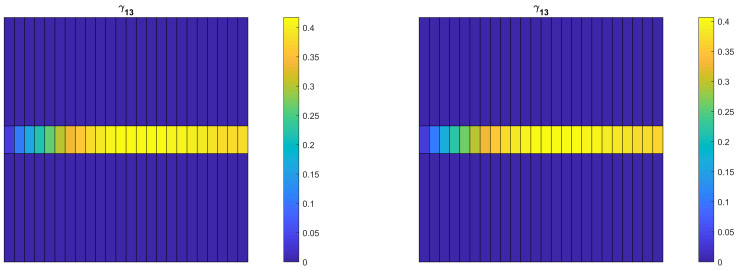

solid-shell constrained solid-shell

Figure 6: Cantilever beam under transverse load: stress component σ_{11} (MPa) (1 is the beam axis) and strain component γ_{13} for the case $L3_A$.

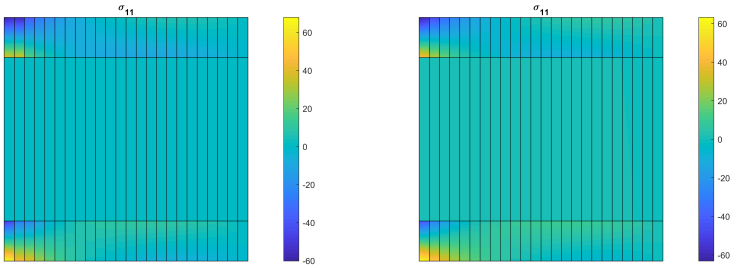

solid-shell constrained solid-shell

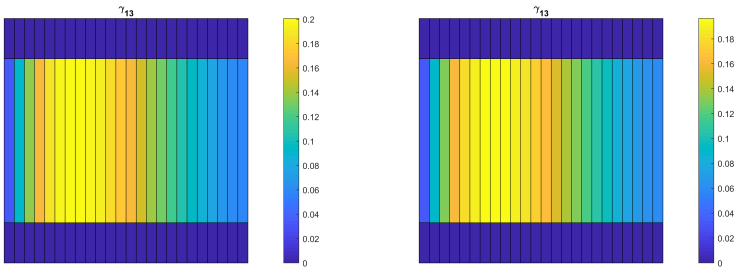

solid-shell constrained solid-shell

Figure 7: Cantilever beam under transverse load: stress component σ_{11} (MPa) (1 is the beam axis) and strain component γ_{13} for the case $L3_B$.

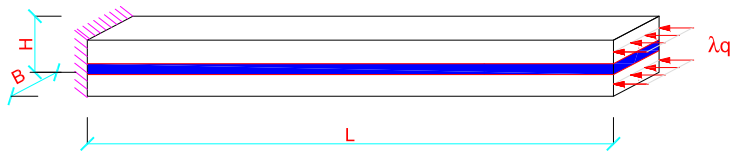

Figure 8: Cantilever beam under compression: geometry, load, and boundary conditions.

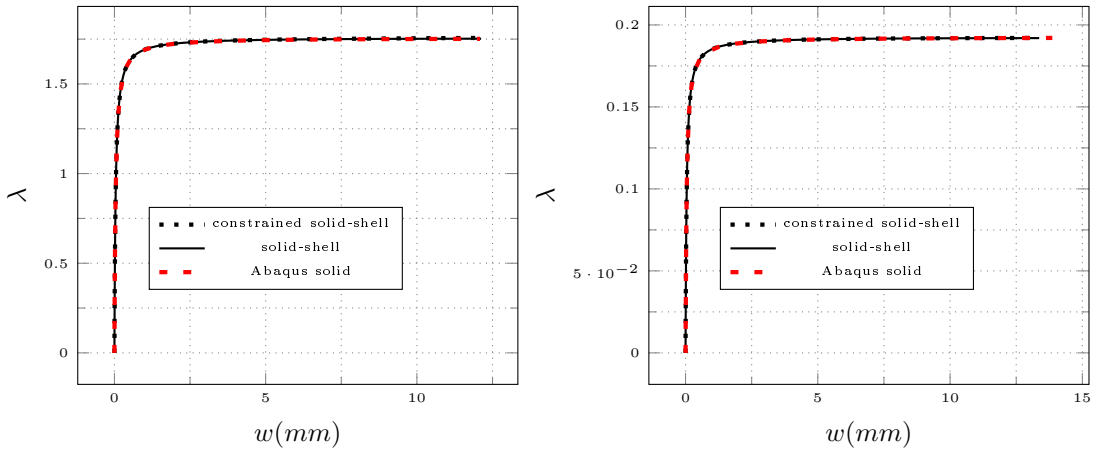

Layup $L3_A$ Layup $L3_B$

Figure 9: Cantilever beam under compression: equilibrium path in terms of vertical tip-displacement component w and comparison between constrained solid-shell and solid-shell model and the results from Abaqus.

4.2. Buckling of a 3-layer cantilever beam under compression

The second test, described in Fig. 8, regards the same cantilever beam seen in the previous test ($L = 500$ mm) but here subject to a compression on the glass layers at the free end point. The layups $L3_A$ and $L3_B$ are considered. The reference surface compression load is $q = 1$ MPa for both the stacking sequences. The solid-shell finite element model consists of 8 elements along the beam axis and only 1 along the width. The perfect structure undergoes buckling with a bifurcation after almost null pre-buckling deformations. A tip out-of-plane imperfection load is then added to avoid the bifurcation jump. The load factor vs. tip transverse displacement curve of the imperfect structure is reported in Fig. 9 for the two stacking sequences and using the different models. It is possible to observe a perfect match between solid-shell model, constrained solid-shell model and the fully solid model up to significant post-buckling deformations, demonstrating the accuracy of the proposed constrained solid-shell modeling. We can note that the buckling load is intermediate between those corresponding to the layered and monolithic limits, proving the need for the intermediate model. Finally, the axial normal stress and the transverse shear strain are depicted in Fig. 10 and Fig. 11 for layup $L3_A$ and $L3_B$, respectively, with the thickness dimension amplified to make the through-the-thickness trend visible. Also in this case, the shear strain is concentrated in the interlayer and varies significantly along the beam axis due to the end effect of the fully clamped boundary condition. The normal stress has a piece-wise linear distribution that is intermediate between monolithic and layered limits, especially for the layup $L3_A$.

4.3. Large deflection of a 3-layer simply supported square plate under transverse load

The large deformation of a simply supported square plate under a transverse load is studied in this test (see Fig. 12). The support is applied on the perimeter of the bottom layer. The layups $L3_A$ and $L3_B$ are used. The reference surface load is $q = 10^{-4}$ MPa for both the stacking sequences and is applied on the

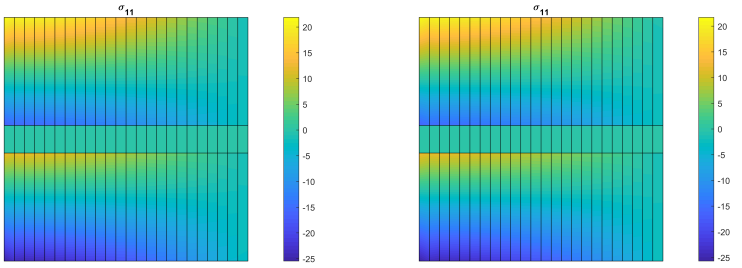

solid-shell constrained solid-shell

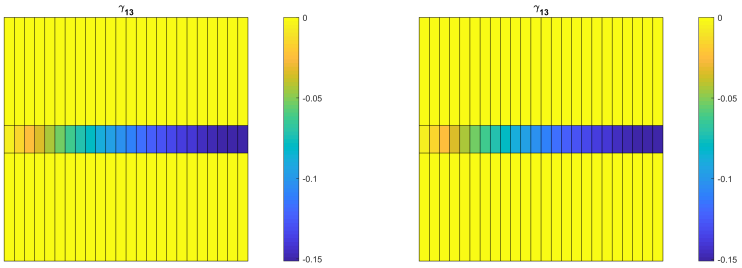

solid-shell constrained solid-shell

Figure 10: Compressed beam: stress component σ_{11} (MPa) (1 is the beam axis) and strain component γ_{13} for layup $L3_A$.

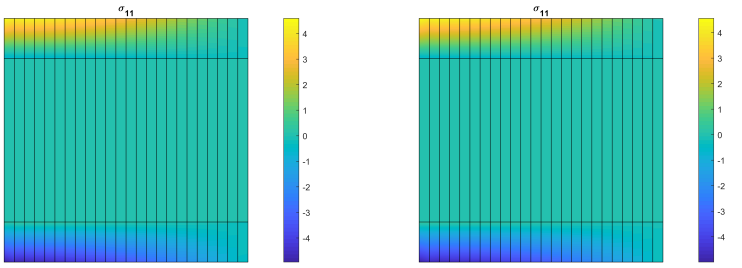

solid-shell constrained solid-shell

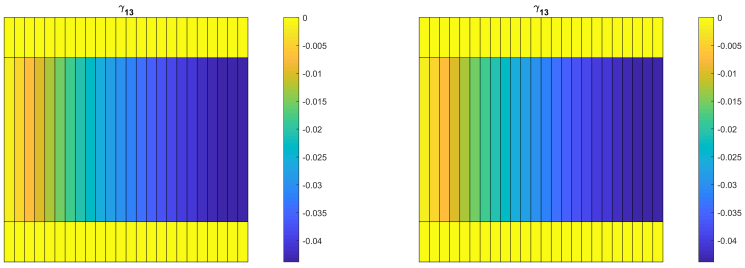

solid-shell constrained solid-shell

Figure 11: Cantilever beam under compression: stress component σ_{11} (MPa) (1 is the beam axis) and strain component γ_{13} for layup $L3_B$.

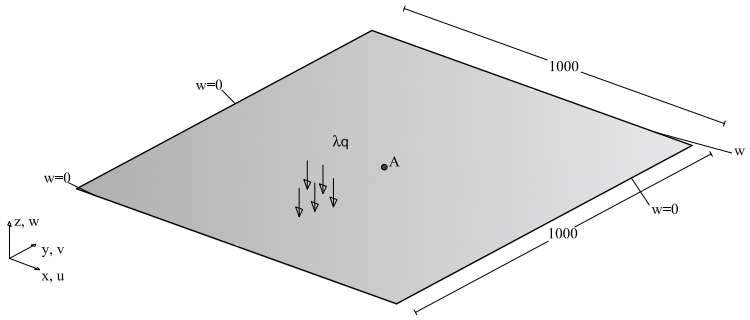

Figure 12: Square plate under transverse load: geometry (mm), load and boundary conditions.

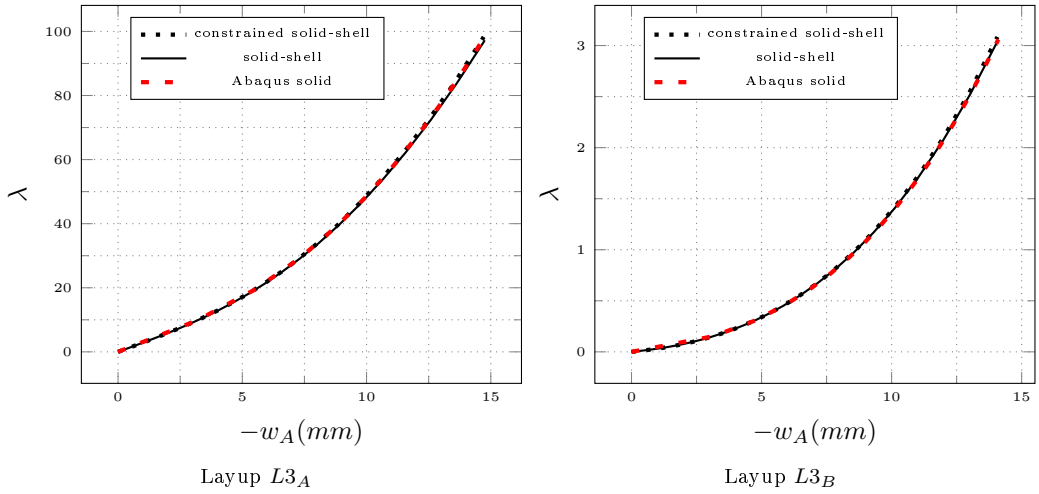

Figure 13: Square plate under transverse load: equilibrium path and comparison between constrained solid-shell and solid-shell model and the results from Abaqus.

top layer. A mesh of 32×32 layered solid-shell elements is used for the in-plane discretization. Figure 13 shows the equilibrium path in terms of load factor vs. the out-of-plane displacement at the center of the plate. It is possible to note the typical increase of the curve slope with the deformation as a consequence of the membrane contribution to the overall stiffness. A perfect match is obtained for the different models, demonstrating again the accuracy of the proposed constrained solid-shell modeling. Also the stress field is accurately reproduced by the proposal as depicted in Fig. 14 and 15, where the stress component σ_{11} is plotted over the top and bottom surfaces of the glass layers and compared to the full solid-shell solution. Also in this test, the stress field is much different with respect to that expected by a monolithic shell model based on the plane section kinematics. Finally, Fig. 16 shows the transverse shear strain γ_{12} concentrated in the interlayer. Again, the thickness direction is amplified in the 3D plot for a better visualization.

4.4. Buckling of a 3-layer simply supported square plate under in-plane shear load

The buckling of the simply supported square plate under a self-equilibrated in-plane shear load is considered in this test for layups $L3_A$ and $L3_B$. Geometry, loads and boundary conditions are illustrated in Fig. 17. The support is applied on the perimeter of the bottom layer. The reference surface load is $q = 1$ MPa for both the stacking sequences and it is applied on the glass layers in the direction parallel to each edge. The adopted discretization consists of 32×32 layered solid-shell elements. A geometric imperfection with the shape of the first linearized buckling mode and an amplitude equal to 0.1 mm is added to the perfect model. The equilibrium path of the imperfect structure is shown in Fig. 18 in terms of out-of-plane

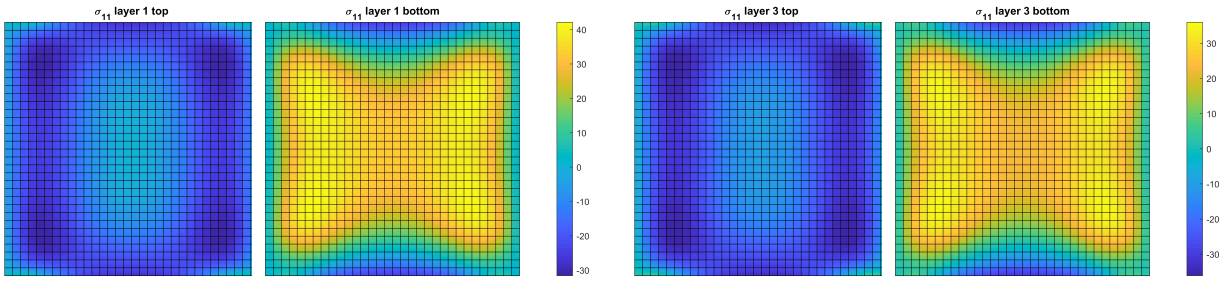

constrained solid-shell

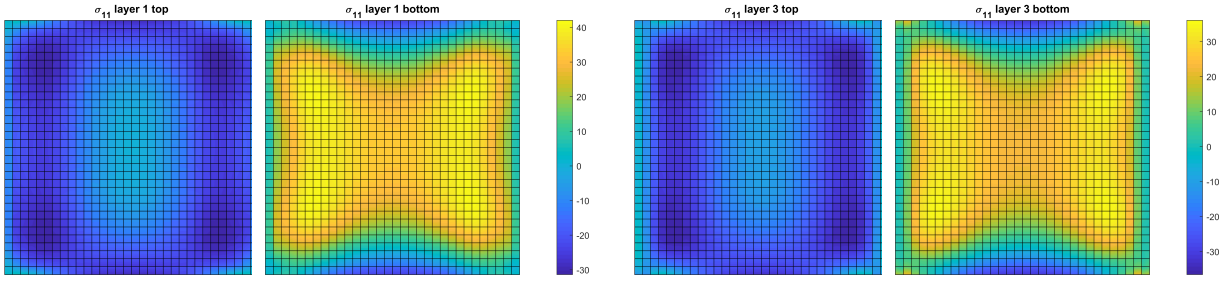

solid-shell

Figure 14: Square plate under transverse load: stress component σ_{11} (MPa) over the glass layers for layup $L3_A$.

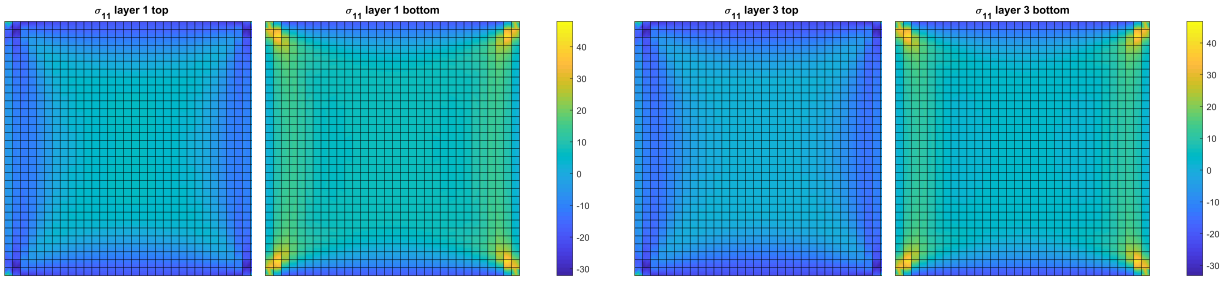

constrained solid-shell

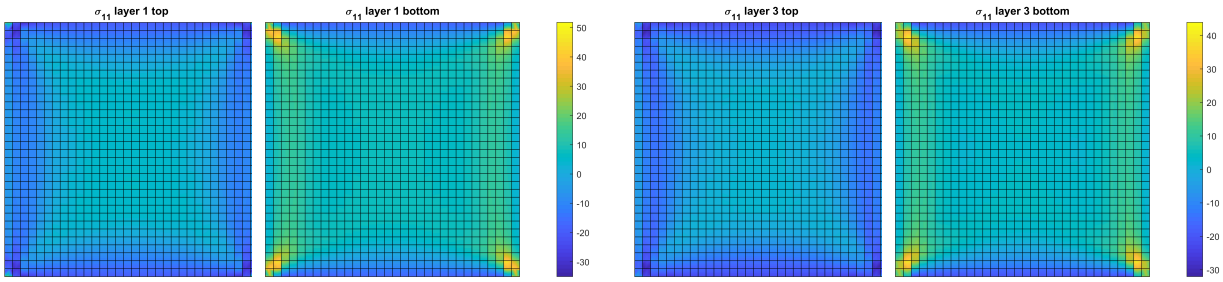

solid-shell

Figure 15: Square plate under transverse load: stress component σ_{11} (MPa) over the glass layers for layup $L3_B$.

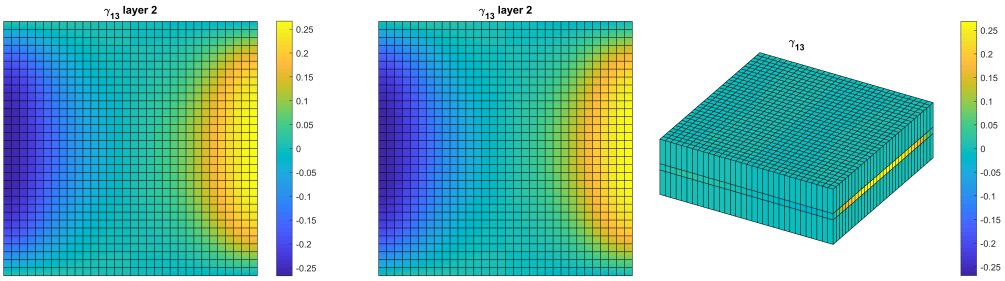

Layup $L3_A$, constrained solid-shell

Layup $L3_A$, solid-shell

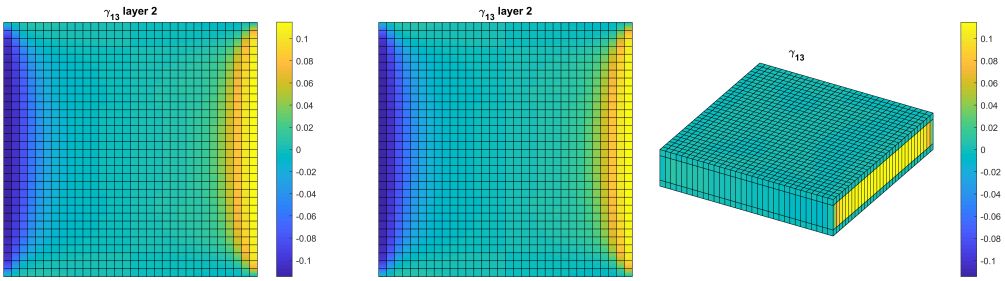

Layup $L3_B$, constrained solid-shell

Layup $L3_B$, solid-shell

Figure 16: Square plate under transverse load: strain component γ_{13} over the interlayer for layup $L3_A$ and $L3_B$.

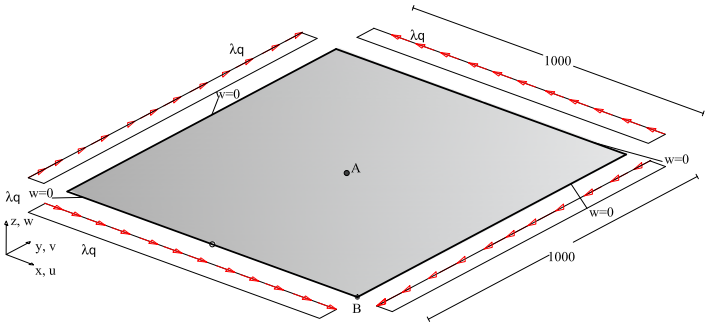

Figure 17: Square plate under transverse load: geometry (mm), load and boundary conditions.

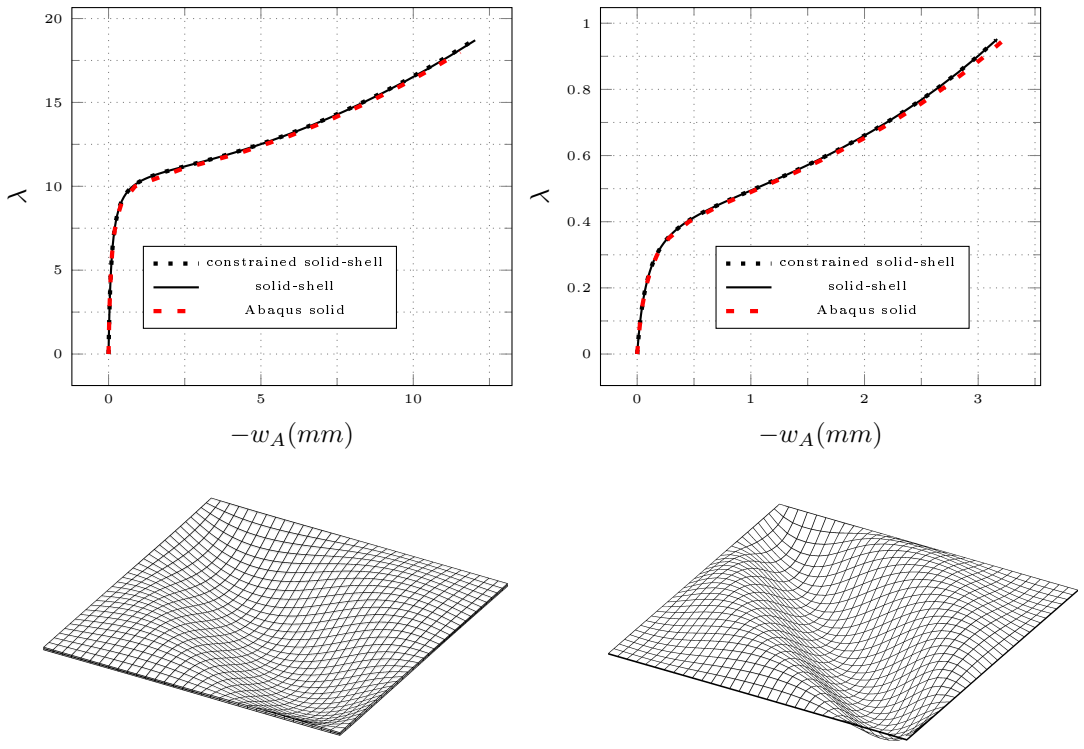

Layup $L3_A$ Layup $L3_B$

Figure 18: Square plate under in-plane shear: equilibrium path and comparison between constrained solid-shell and solid-shell model and the results from Abaqus.

displacement of the plate center. It is possible to note the stiffness reduction after the buckling point, with a smooth change due to the imperfection. An excellent match is obtained for the different models. In the same figure, the post-buckled deformed configurations at the last equilibrium point are also available. This holds also for the stress field, whose component σ_{11} is shown in Figs. 19 and 20 for the two layups, according to the solid-shell and constrained solid-shell models. Finally, the transverse shear strain γ_{12} in the interlayer is reported in Fig. 21, with the thickness direction amplified in the 3D plot for a better visualization.

4.5. 5-layer rectangular plate simply supported on 4 edges under compression

A rectangular simply supported plane made of five alternating layers (layup $L5$) is now considered under two different loading cases: an out-of-plane load distributed over the plate and an axial compression load distributed on the short edges. Geometry, loads and boundary conditions are depicted in Fig. 22. The support is assigned on the perimeter of the bottom layer. The reference surface load is $q = 10^{-3}$ MPa for the transverse load case applied on the top layer, while $q = 1$ MPa as surface load distributed on glass layers in the compression test. A geometric imperfection with the shape of the first linearized buckling mode, with maximum deviation equal to 0.1 mm, is introduced for the second load case to nudge the structure on the bifurcated path. The equilibrium paths are plotted in Fig. 23 and are characterized by large deflections and buckling for the two load conditions respectively. The deformed configurations at the last equilibrium point are also shown. The curves are reported for the different models, demonstrating also in this 5-layer case the accuracy of the proposed constrained solid-shell finite element with a reduced number of unknowns.

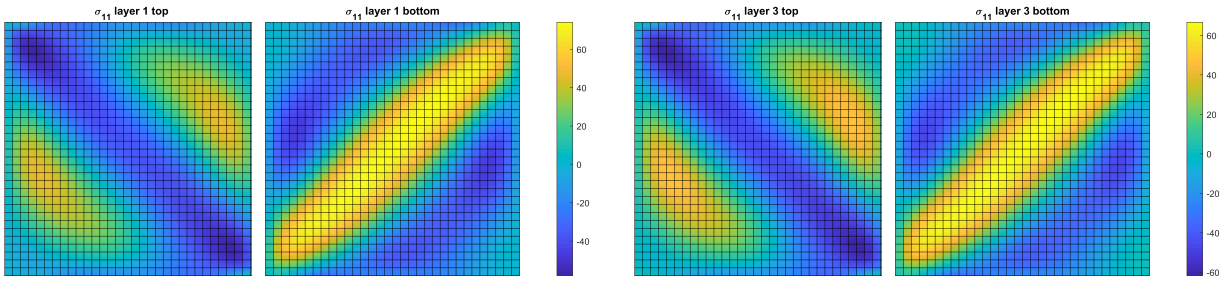

constrained solid-shell

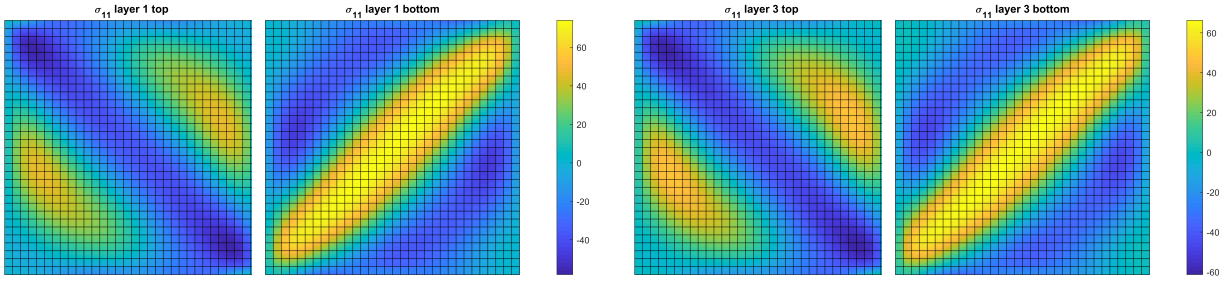

solid-shell

Figure 19: Square plate under in-plane shear: stress component σ_{11} (MPa) over the glass layers for layup $L3_A$.

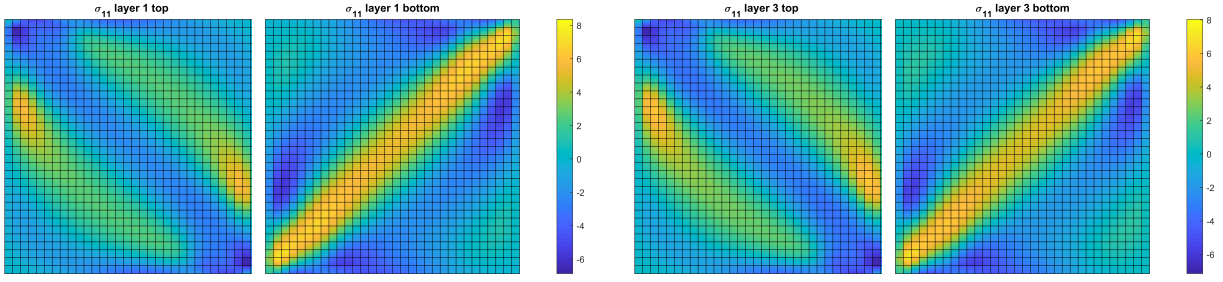

constrained solid-shell

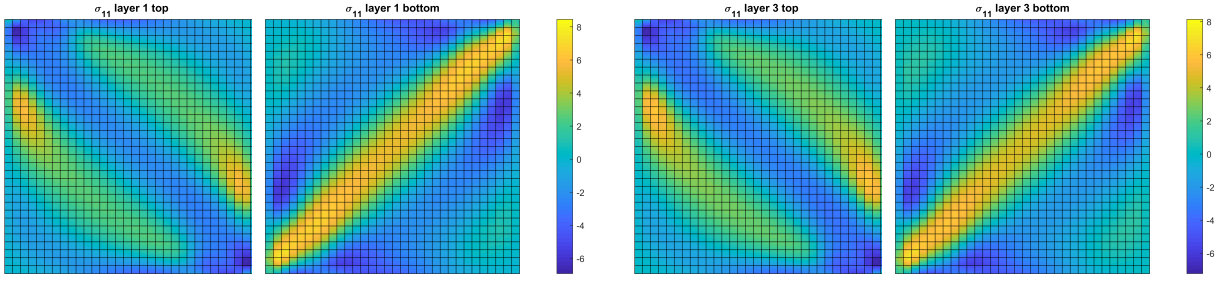

solid-shell

Figure 20: Square plate under in-plane shear: stress component σ_{11} (MPa) over the glass layers for layup $L3_B$.

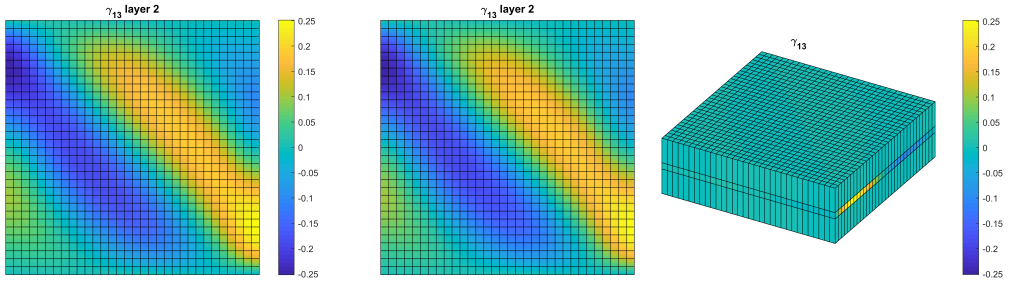

Layup $L3_A$, constrained solid-shell Layup $L3_A$, solid-shell

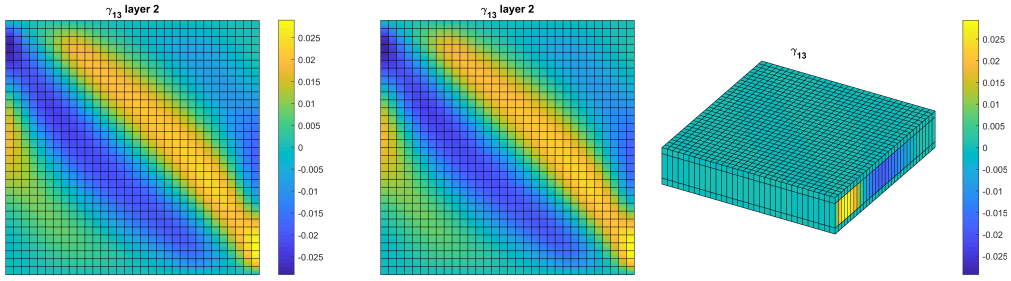

Layup $L3_B$, constrained solid-shell Layup $L3_B$, solid-shell

Figure 21: Square plate under in-plane shear: strain component γ_{13} over the interlayer for layup $L3_A$ and $L3_B$.

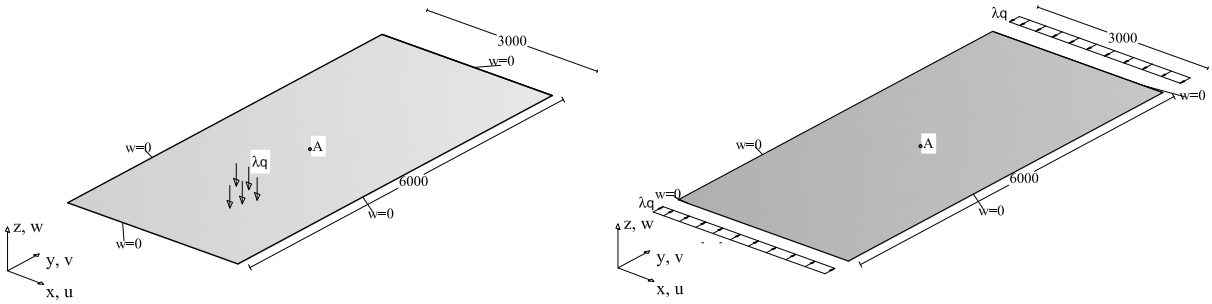

Transverse load Axial compression

Figure 22: Rectangular plate: geometry (mm), loads and boundary conditions.

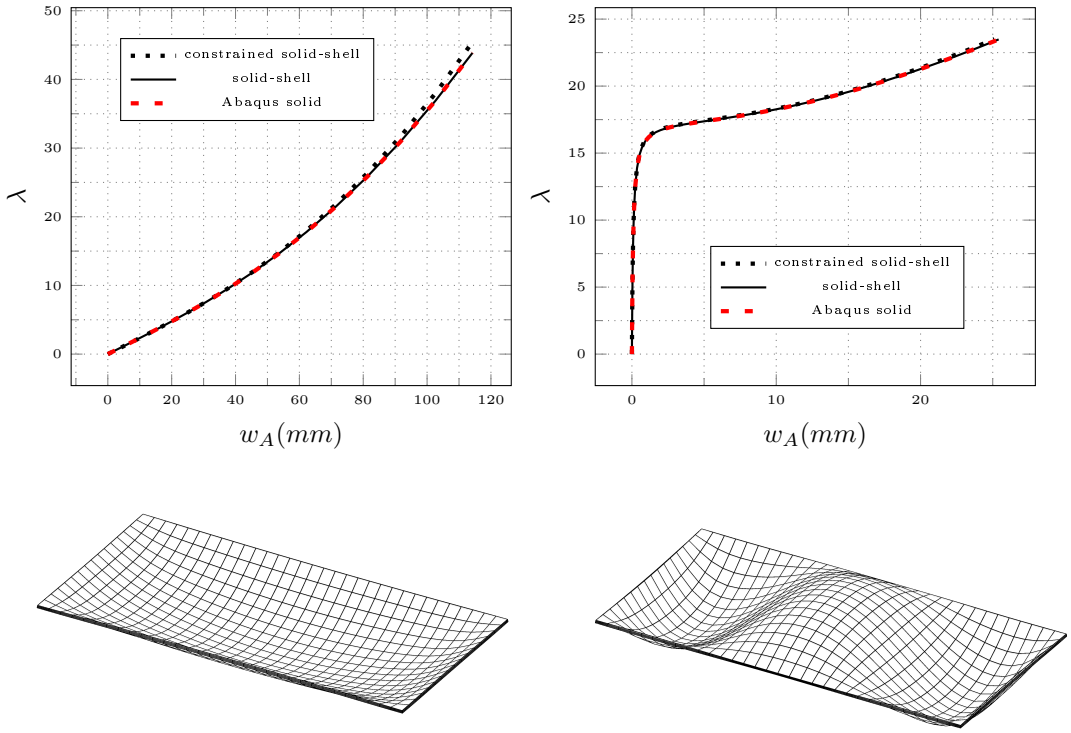

Transverse load

Axial compression

Figure 23: Rectangular plate: equilibrium path and comparison between constrained solid-shell and solid-shell model and the results from Abaqus, for two load cases.

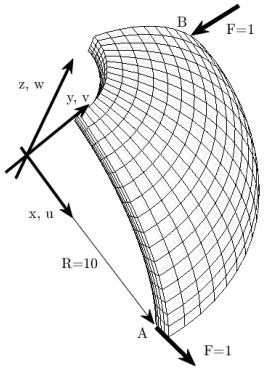

Figure 24: Hemispherical shell: geometry and applied loads.

Layer Index	Layer Material	Layer thickness		
		L1	L2	L3
1	(F)	1/5h	1/15h	3/25h
2	(C)	1/5h	2/15h	5/25h
3	(F)	1/5h	3/15h	9/25h
4	(C)	1/5h	4/15h	5/25h
5	(F)	1/5h	5/15h	3/25h

Table 1: Hemispherical shell analyzed in [21]: description of the three lay-ups, referred to as L1, L2 and L3.

4.6. Multi-layer hemispherical shell with 18° cut-off

To test the accuracy of our proposed model also for curved structures, we evaluate the equilibrium paths of a 5-layer hemispherical shell with a circular cut-off at its top, as reported in Fig. 24. This exactly replicates, for the sake of comparison, the same geometry, loads and material layups considered in [21]. The input data are given in non-dimensional form, as in [21]. The hole aperture is 18°, the sphere radius is 10, and the shell thickness is $h = 0.075$. Three alternative lay-ups are considered presenting both symmetric and asymmetric cross-sections. The layer material type and thickness for each lay-up are listed in Tab. 1, where layer (1) corresponds to the interior layer of the hemispherical shell. The material parameters for the stiff layers (F) and soft layers (C) are: $E_F = 1.0 \times 10^7$, $E_C = 5.0 \times 10^3$ and $\nu_F = \nu_C = 0.2$. The shell is subject to symmetric concentrated forces at its base, increased according to the load multiplier λ.

Due to symmetry, only one quarter of the shell is modeled, evaluating the results obtained with 3 different meshes, respectively of 8×8, 16×16 and 32×32 solid-shell elements. For all the considered laminated packages, it is possible to observe as the coarsest meshes of 8×8 solid-shell elements furnish very accurate solutions, while no differences can be observed between the 16×16 and 32×32 grids. The results are in good agreement with those proposed in [21], where a discretization of 16×16 quadratic corotational elements is employed. This confirms the accuracy of our proposal, which is competitive with quadratic corotational elements also for curved structures despite our cheaper linear interpolation (lower number of DOFs per given mesh and reduced sparsity), also thanks to the Total Lagrangian geometrically exactness of the model. Finally, no significant differences between constrained and unconstrained models have been observed also in this test. However, convergence difficulties in the iterative process affect the unconstrained model, for very high load amplifiers.

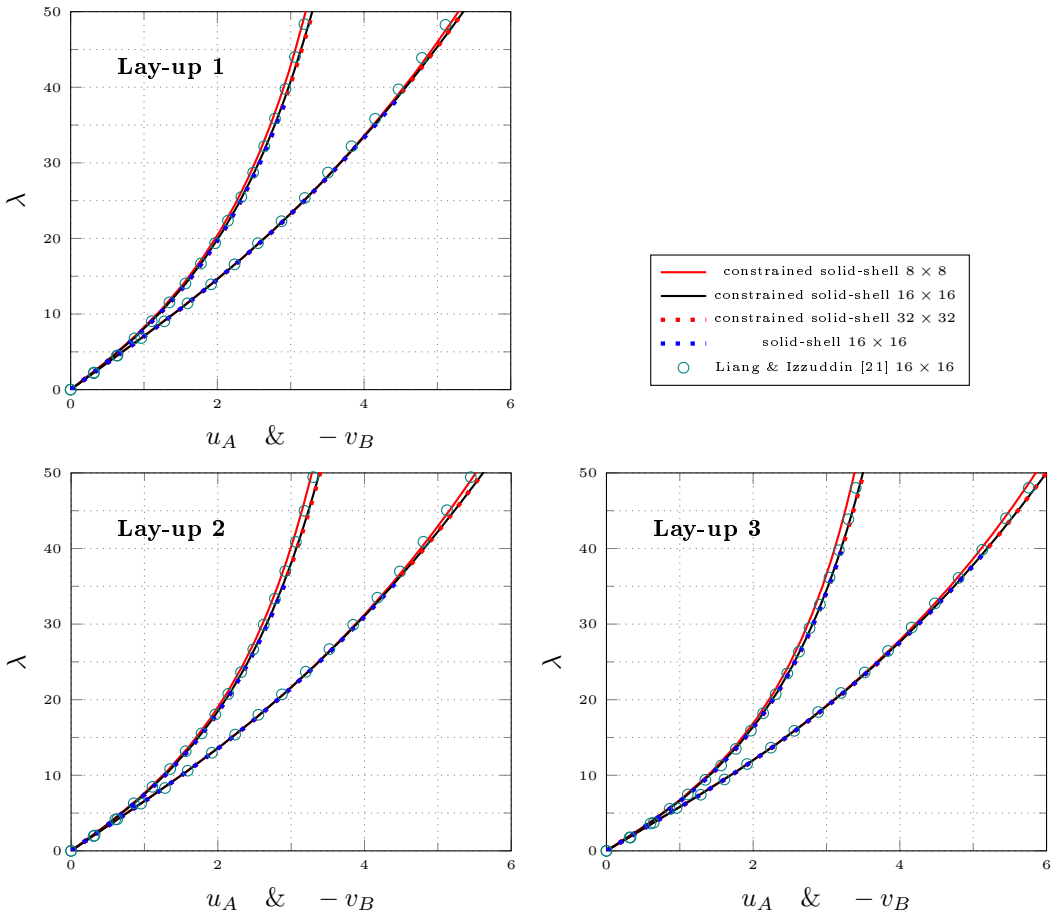

Figure 25: Equilibrium paths for the hemispherical shell: comparison of the constrained-solid-shell and solid-shell models with the results from [21], for lay-up L1, L2 and L3.

5. Conclusions

We have presented two types of solid-shell finite-element models for laminated plates made of alternating stiff/soft layers, amenable of large deflections and buckling. Although the potential range of applications is much wider, laminated glass has been considered as a relevant engineering example, as it is characterized by stiff glass plies of various thickness, permanently bonded by soft polymeric interlayers, with different thickness and stiffness. For these class of composites homogenized models, such as those derived from the first order lamination theory, result inaccurate because of the cross-sectional warping, consequent to the significant transverse shear strains concentrated in the soft layers. The first considered case is represented by a layered solid-shell model, where one solid-shell element, with linear through-the-thickness approximation, is adopted for each layer in the thickness direction. This model is based on a Total Lagrangian solid description with a geometrically exact Green-Lagrange strain measure in terms of the top and bottom displacement of each layer, with the C^0 continuity directly enforced on the discrete DOFs. The constitutive law is expressed in stress resultants in order to avoid the through-the-thickness numerical integration. The second model consists in a reduction of the first kinematic model via a further internal constraint, entailing equal finite rotation of the stiff layers at each surface point. The second approach is more efficient than the first one, thanks to the reduced number of unknowns. It maintains the simplicity of the displacement-based solid-shell, because the finite rotation constraint is imposed directly by a linear combination of the nodal displacement DOFs and a constitutive matrix enforcing the plane stress condition. Extensive numerical experiments demonstrated the accuracy of the reduced modeling in paradigmatic case-studies, under large deformation and buckling.

The two models have been presented for the most general cases of multi-laminated curved shells. The worked examples have considered various three- and five-layered flat plates and one curved shell under increasing loading. A further improvement will consist in considering the viscoelastic character of the interlayers, in order to evaluate the variation over time of the degree of coupling between the glass plies. In this way, it will also be possible to study other types of current problems in glass engineering, such as those related to the cold-bending and cold-lamination-bending of laminated glass.

In all cases, we believe that the proposed solid-shell finite-element formulation presents significant advantages over the usual description with 3D models, which requires considerable computational effort, as well as over commercial software commonly used in the design practice, which have significant limitations.

Acknowledgment

Domenico Magisano and Giovanni Garcea were partially supported by the Italian Ministry of University and Research (P.R.I.N. National Grant 2017, Project code 2017J4EAYB; University of Calabria Research Unit). Gianni Royer Carfagni was partially supported by the Italian Department of Civil Protection, within the ReLUIS-DPC 2019 – 2021 Research Project.

Data availability statement

The authors confirm that the data supporting the findings of this study are available within the article.

References

[1] J. Reddy, Mechanics of Laminated Composite Plates and Shells: Theory and Analysis (2nd ed.), CRC Press, 2003. doi:https://doi.org/10.1201/b12409.

[2] A. Ferreira, G. Fasshauer, R. Batra, J. Rodrigues, Static deformations and vibration analysis of composite and sandwich plates using a layerwise theory and rbf-ps discretizations with optimal shape parameter, Composite Structures 86 (4) (2008) 328–343. doi:https://doi.org/10.1016/j.compstruct.2008.07.025.

[3] C. H. Thai, A. Ferreira, E. Carrera, H. Nguyen-Xuan, Isogeometric analysis of laminated composite and sandwich plates using a layerwise deformation theory, Composite Structures 104 (2013) 196–214. doi:https://doi.org/10.1016/j.compstruct.2013.04.002.

[4] Y. Cho, R. Averill, First-order zig-zag sublaminate plate theory and finite element model for laminated composite and sandwich panels, Composite Structures 50 (1) (2000) 1–15. doi:https://doi.org/10.1016/S0263-8223(99)00063-X.

[5] E. Carrera, Historical review of Zig-Zag theories for multilayered plates and shells, Applied Mechanics Reviews 56 (3) (2003) 287–308. doi:https://doi.org/10.1115/1.1557614.
[6] L. Demasi, Refined multilayered plate elements based on murakami zig-zag functions, Composite Structures 70 (3) (2005) 308–316. doi:https://doi.org/10.1016/j.compstruct.2004.08.036.
[7] M. Martín, X. Centelles, A. Solé, C. Barreneche, A. I. Fernández, L. F. Cabeza, Polymeric interlayer materials for laminated glass: A review, Construction and Building Materials 230 (2020) art. n. 116897. doi:https://doi.org/10.1016/j.conbuildmat.2019.116897.
[8] Dow®, DOWSIL^{TM} 9955 Encapsulation and Lamination Silicone (2022).
URL https://www.dow.com/en-us/pdp.dowsil-9955-encapsulation-and-lamination-silicone.510092z.
[9] L. Biolzi, S. Cattaneo, M. Orlando, L. R. Piscitelli, P. Spinelli, Constitutive relationships of different interlayer materials for laminated glass, Composite Structures 244 (2020) art. n. 112221. doi:https://doi.org/10.1016/j.compstruct.2020.112221.
[10] R. Schapery, A method of viscoelastic stress analysis using elastic solutions, Journal of the Franklin Institute 279 (4) (1965) 268–289. doi:https://doi.org/10.1016/0016-0032(65)90339-X.
[11] H. S. Norville, K. W. King, J. L. Swofford, Behavior and strength of laminated glass, Journal of Engineering Mechanics 124 (1) (1998) 46 – 53. doi:10.1061/(ASCE)0733-9399(1998)124:1(46).
[12] L. Galuppi, E. Riva, Experimental and numerical characterization of twisting response of thin glass, Glass Structures and Engineering 7 (1) (2022) 45–69. doi:https://doi.org/10.1007/s40940-022-00166-0.
[13] G. Coult, The skypool: bringing architectural imagination to life, Glass Structures and Engineering 6 (3) (2021) 353–373. doi:https://doi.org/10.1007/s40940-021-00158-6.
[14] N. Krishnamoorthy, S. Nayak, G. K. Surisetty, M. Chaturvedi, S. Shuler, Polycarbonate glazing body panels for automotive applications, SAE Technical Papers 2009-January (January) (2009). doi:https://doi.org/10.4271/2009-26-0085.
[15] M. Ito, Y. Masuda, K. Nagai, Evaluation of long-term stability and degradation on polycarbonate based plastic glass, Journal of Polymer Engineering 35 (1) (2015) 31 – 40. doi:10.1515/polyeng-2014-0085.
[16] J. Hänig, B. Weller, Experimental investigations and numerical simulations of innovative lightweight glass-plastic-composite panels made of thin glass and pmma, Glass Structures and Engineering 6 (2) (2021) 249–271. doi:https://doi.org/10.1007/s40940-021-00153-x.
[17] Y. Liang, B. Izzuddin, Nonlinear analysis of laminated shells with alternating stiff/soft lay-up, Composite Structures 133 (2015) 1220–1236. doi:https://doi.org/10.1016/j.compstruct.2015.08.043.
[18] I. V. Ivanov, D. S. Velchev, N. G. Georgiev, I. D. Ivanov, T. Sadowski, A plate finite element for modelling of triplex laminated glass and comparison with other computational models, Meccanica 51 (2016) 341–358. doi:https://doi.org/10.1007/s11012-015-0275-0.
[19] D. Bohmann, SJ Software GmbH Aachen, title = SJ Mepla Theory Manual, Version 5.0, year = 2018, address = Aachen,.
[20] C. Felippa, B. Haugen, A unified formulation of small-strain corotational finite elements: I. theory, Computer Methods in Applied Mechanics and Engineering 194 (21) (2005) 2285–2335. doi:https://doi.org/10.1016/j.cma.2004.07.035.
[21] Y. Liang, F. Lancaster, B. Izzuddin, Effective modelling of structural glass with laminated shell elements, Composite Structures 156 (2016) 47–62, 70th Anniversary of Professor J. N. Reddy. doi:https://doi.org/10.1016/j.compstruct.2016.02.077.
[22] L. Leonetti, D. Magisano, A. Madeo, G. Garcea, J. Kiendl, A. Reali, A simplified Kirchhoff-Love large deformation model for elastic shells and its effective isogeometric formulation, Computer Methods in Applied Mechanics and Engineering 354 (2019) 369 – 396. doi:https://doi.org/10.1016/j.cma.2019.05.025.
[23] A. J. Herrema, E. L. Johnson, D. Proserpio, M. C. Wu, J. Kiendl, M.-C. Hsu, Penalty coupling of non-matching isogeometric Kirchhoff-Love shell patches with application to composite wind turbine blades, Computer Methods in Applied Mechanics and Engineering 346 (2019) 810–840. doi:https://doi.org/10.1016/j.cma.2018.08.038.
[24] A. Nitti, J. Kiendl, A. Gizzi, A. Reali, M. D. de Tullio, A curvilinear isogeometric framework for the electromechanical activation of thin muscular tissues, Computer Methods in Applied Mechanics and Engineering 382 (2021) 113877. doi:https://doi.org/10.1016/j.cma.2021.113877.
[25] K. Sze, W. Chan, T. Pian, An eight-node hybrid-stress solid-shell element for geometric non-linear analysis of elastic shells, International Journal for Numerical Methods in Engineering 55 (7) (2002) 853–878. doi:http://dx.doi.org/10.1002/nme.535.
[26] M. Schwarze, S. Reese, A reduced integration solid-shell finite element based on the EAS and the ANS concept-Large deformation problems, International Journal for Numerical Methods in Engineering 85 (3) (2011) 289–329. doi:https://doi.org/10.1002/nme.2966.
[27] Q. Li, Y. Liu, Z. Zhang, W. Zhong, A new reduced integration solid-shell element based on EAS and ANS with hourglass stabilization, International Journal for Numerical Methods in Engineering (2015) 1885–1891arXiv:1010.1724, doi:http://dx.doi.org/10.1002/nme.
[28] L. Leonetti, F. Liguori, D. Magisano, G. Garcea, An efficient isogeometric solid-shell formulation for geometrically nonlinear analysis of elastic shells, Computer Methods in Applied Mechanics and Engineering 331 (2018) 159 – 183. doi:https://doi.org/10.1016/j.cma.2017.11.025.
[29] D. Magisano, L. Leonetti, A. Madeo, G. Garcea, A large rotation finite element analysis of 3D beams by incremental rotation vector and exact strain measure with all the desirable features, Computer Methods in Applied Mechanics and Engineering 361 (2020) 112811. doi:https://doi.org/10.1016/j.cma.2019.112811.
[30] A. Ibrahimbegovic, On the choice of finite rotation parameters, Computer Methods in Applied Mechanics and Engineering 149 (1) (1997) 49–71, containing papers presented at the Symposium on Advances in Computational Mechanics. doi:https://doi.org/10.1016/S0045-7825(97)00059-5.
[31] J. Simo, D. Fox, On a stress resultant geometrically exact shell model. part i: Formulation and optimal parametrization, Computer Methods in Applied Mechanics and Engineering 72 (3) (1989) 267–304. doi:https://doi.org/10.1016/0045-

7825(89)90002-9.
[32] H. Naceur, S. Shiri, D. Coutellier, J. Batoz, On the modeling and design of composite multilayered structures using solid-shell finite element model, Finite Elements in Analysis and Design 70-71 (2013) 1–14. doi:https://doi.org/10.1016/j.finel.2013.02.004.
[33] P. Lenk, H. Lambert, Practical aspects of finite-element analysis in structural glass design, Proceedings of the Institution of Civil Engineers - Structures and Buildings 168 (7) (2015) 527–538. doi:10.1680/stbu.13.00104.
[34] M. Bischoff, E. Ramm, Shear deformable shell elements for large strains and rotations, International Journal for Numerical Methods in Engineering 40 (23) (1997) 4427–4449. doi:https://doi.org/10.1002/(SICI)1097-0207(19971215)40:23<4427::AID-NME268>3.0.CO;2-9.
[35] D. Magisano, L. Leonetti, G. Garcea, Koiter asymptotic analysis of multilayered composite structures using mixed solid-shell finite elements, Composite Structures 154 (2016) 296–308. doi:10.1016/j.compstruct.2016.07.046.
[36] T. H. H. Pian, C.-C. Wu, Hybrid and Incompatible Finite Element Methods, Chapman & All, CRC, New-York, 1969.
[37] D. Magisano, L. Leonetti, G. Garcea, Advantages of the mixed format in geometrically nonlinear analysis of beams and shells using solid finite elements, International Journal for Numerical Methods in Engineering 109 (9) (2017) 1237–1262. doi:10.1002/nme.5322.
[38] D. Magisano, L. Leonetti, G. Garcea, How to improve efficiency and robustness of the Newton method in geometrically non-linear structural problem discretized via displacement-based finite elements, Computer Methods in Applied Mechanics and Engineering 313 (2017) 986 – 1005. doi:http://dx.doi.org/10.1016/j.cma.2016.10.023.